RADIOFREQUENCY COIL DESIGN FOR MAGNETIC RESONANCE IMAGING

AND SPECTROSCOPY OF THE HUMAN BREAST AND MODELS OF

DUCHENNE MUSCULAR DYSTROPHY

A Dissertation

by

ROMINA DEL BOSQUE

Submitted to the Office of Graduate and Professional Studies of
Texas A&M University
in partial fulfillment of the requirements for the degree of

DOCTOR OF PHILOSOPHY

Chair of Committee,	Mary P. McDougall
Committee Members,	Kristen Maitland
	Steven M. Wright
	Peter Nghiem
Head of Department,	Mike McShane

May 2020

Major Subject: Biomedical Engineering

ABSTRACT

The known value of magnetic resonance imaging and spectroscopy (MRI/MRS) to detect and monitor disease with high sensitivity has driven researchers and clinicians to continually push boundaries beyond clinically-standard ^{1}H MRI. This has led to many advancements including high field MRI and MRS and non-^{1}H MRI and MRS.

MRI of the breast is commonly used as a supplemental tool to mammography throughout various stages of diseases. Specifically, benefits of high field MRI and the use of array coils have enabled studies such as dynamic contrast enhanced MRI (DCE-MRI) and diffusion weighted imaging (DWI) with high spatial and/or temporal resolution. These studies provide additional information about morphology and kinetics of breast lesions to distinguish between malignant and benign tumors with improved diagnostic accuracy.

MR imaging and spectroscopy have been used to study progressive muscular degenerative disorders, such as Duchenne muscular dystrophy (DMD). ^{1}H MRI has been used to assess skeletal muscle composition, such as muscle fat-fraction. Additionally, ^{23}Na imaging and ^{31}P spectroscopy have provided supplementary information pertaining to tissue viability and metabolic function to evaluate disease even before any measurable change in muscle composition has occurred.

This dissertation covers the construction and characterization of radiofrequency (RF) coils and corresponding hardware to enable studies pertaining to breast cancer and DMD. A 32-channel breast array and modified forced-current excitation (FCE) volume

coil was constructed for bilateral breast imaging at 7T. Ultimately, coil performance was evaluated based on improvements in SNR and feasibility of accelerated, high spatial resolution imaging. Two double-tuned birdcage coils ($^1H/^{23}Na$ and $^1H/^{31}P$) were constructed for imaging and spectroscopy at 4.7T of rectus femoris muscles excised from genetically-homologous animal models of DMD, or golden retriever muscular dystrophy (GRMD). Initially, coil performance was evaluated on various phantoms for homogeneity and ability to distinguish between various biological concentrations of sodium and phosphorus. The coils were then used to collect data from a variety of GRMD tissue samples in order to characterize biomarkers corresponding to age/disease progression. Overall, this work has contributed hardware advancements to enable MRI/MRS studies beyond clinically-standard ^1H MRI to assess disease.

ACKNOWLEDGEMENTS

CONTRIBUTORS AND FUNDING SOURCES

This work was supervised by a dissertation committee consisting of: Dr. Mary McDougall (committee chair), Dr. Steven M. Wright, Dr. Kristen Maitland, and Dr. Peter Nghiem.

The volume coil outlined in Chapter 2 was constructed by colleague, Dr. Jiaming Cui of the Department of Electrical Engineering. One of the two double-tuned birdcage coils presented in Chapter 3 was constructed by an undergraduate student of the Department of Biomedical Engineering, Edith Valle. The ^{31}P spectra presented in Chapter 4 was post-processed in a custom Matlab program made by colleague, Travis Carrell of the Department of Biomedical Engineering.

All other work presented in this dissertation was completed by the student independently.

Funding Sources

NOMENCLATURE

^{1}H	Hydrogen atom
^{23}Na	Sodium-23 isotope
^{31}P	Phosphorus-31 isotope
7T	Adjective indicating B_0 = 7 Tesla
AP	Anterior-posterior
B_0	Static magnetic flux density
B_1^+	Circularly-polarized transmit B_1
CVP	Common voltage point
DCE-MRI	Dynamic contrast enhanced MRI
DMD	Duchenne muscular dystrophy
DWI	Diffusion weighted imaging
FCE	Forced current excitation
HF	Head-foot
GEMS	Gradient echo multi-slice
g-factor	Geometry factor in parallel imaging
GRMD	Golden retriever muscular dystrophy
MRI	Magnetic resonance imaging
MRS	Magnetic resonance spectroscopy
NMR	Nuclear magnetic resonance
PCB	Printed circuit board

PCr	Phosphocreatine
PDE	Phosphodiesters
Pi	Inorganic phosphate
Q	Quality- factor
R	Acceleration factor in parallel imaging
RF	Radiofrequency
ROI	Region-of-interest
S_{11}	Reflection coefficient
S_{12}	Transmission coefficient
SAR	Specific absorption rate
SD	Scan duration
SEMS	Spin echo multi-slice
SNR	Signal-to-noise ratio
SPULS	1-D Pulse and acquire sequence
T1w	T_1 weighted
T2w	T_2 weighted
TE	Echo time
TR	Repetition time
TSC	Total sodium concentration

TABLE OF CONTENTS

LIST OF FIGURES

Page

LIST OF TABLES

CHAPTER I

INTRODUCTION

I.1 Background and Significance

Since the early works of Paul Lauterbur and Peter Mansfield in the 1970s [1,2],

many advancements have been made in magnetic resonance imaging (MRI) and

magnetic resonance spectroscopy (MRS) research, showing the vast potential of these

techniques for diagnosing and evaluating various diseases. The known value of these

techniques has driven researchers and clinicians to continually push boundaries beyond

clinically-standard ^{1}H MRI, leading to many advancements including ultra-high field

MRI and MRS and non-^{1}H MRI and MRS. However, to perform these non-standard

studies, specialized hardware such as custom radiofrequency (RF) coils is often required.

This work describes various types of custom RF coils and additional hardware

constructed to enable studies of disease, specifically breast cancer and Duchenne

muscular dystrophy (DMD).

In 2019, over 200,000 new cases of breast cancer were reported, making it the

most commonly diagnosed cancer in the United States [3]. MRI of the breast is

commonly used as a supplemental tool to mammography throughout various stages of

disease, from screening to recurrence, because of its ability to detect breast lesions with

high sensitivity irrespective of dense breast tissue [4-8]. Furthermore, studies such as

dynamic contrast-enhanced (DCE) MRI and diffusion weighted imaging (DWI) can be

used to differentiate between malignant and benign tumors with improved diagnostic

accuracy (9-13). Because of the dynamic nature of these studies, it is important to acquire images quickly while simultaneously maintaining spatial resolution and image quality. Therefore, these studies can greatly benefit from the use of RF coil arrays at high magnetic fields (such as 7T) because the increase in signal-to-noise ratio provided can be used to increase both temporal and spatial resolution (14-18). Benefits provided by a 32-channel receive array at 7T will be discussed in detail in Chapter 2.

Similarly, MRI and MRS have been used to study progressive muscular disorders such as DMD, showing vast potential in noninvasively evaluating disease throughout various stages (19-30). However, the studies are mostly limited to ^{1}H imaging and spectroscopy (21-24) largely because of the reduced availability of non-^{1}H hardware, i.e. RF coils, used to perform X-nuclei MR experiments. Despite these limitations, potentially valuable biomarkers have been observed using ^{23}Na imaging (25-27) and ^{31}P spectroscopy (28-30). Two double-tuned RF coils and corresponding hardware have been developed to enable studies on formalin-fixed rectus femoris muscles of a genetically homologous animal model, the golden retriever muscular dystrophy (GRMD) model, as discussed in Chapter 3. Furthermore, assessments on the effects of age/disease progression on specific biomarkers are examined in Chapter 4.

I.1.1 NMR Background

Nuclear magnetic resonance (NMR) is the phenomenon used in both MR imaging and MR spectroscopy. This phenomenon describes how NMR-active nuclei act in the presence of an external magnetic field and how changes to the nuclei's orientation produce a detectable RF signal. For simplicity of this explanation, it is assumed that the

2

nuclei of interest are that of hydrogen, abundant in the high water content in the human body and used for all clinical "proton" imaging. When protons are outside of an external magnetic field, or outside an MRI system, they are randomly oriented. However, when subjected to an external magnetic field, nuclei change their orientation where their angular momentum vector is either parallel or antiparallel with the main magnetic field B_0, as shown in Figure I-1. These two possible orientations, or spin-states, can be explained by the difference in energy between both spin-states, with the lower energy state (parallel to B_0) always having a slight excess in comparison to the high energy state (antiparallel to B_0) state. This slight excess, often referred to as net magnetization (M_0), contributes to the overall achievable signal and is proportional to the strength of the external magnetic field, meaning higher magnetic fields increase achievable signal (31).
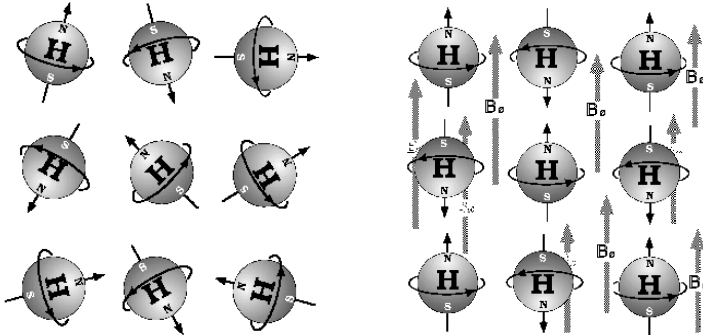
Figure I-1. Orientations of protons outside and in an external magnetic field. Protons are randomly oriented without the presence of an external magnetic field (left). When placed in a magnetic field, protons align parallel or anti-parallel to B_0 (right). Reprinted with permission from (31).

Once protons are aligned with or against the main magnetic field, they precess about their axis at a frequency often referred to as the Larmor frequency (ω_0). The Larmor frequency (ω_0) is dependent on the strength of the main magnetic field (B_0) and the gyromagnetic ratio of the nuclei of interest (γ), as shown in Eq I.1.

$$\omega_0 = B_0\gamma \qquad \text{(Eq I.1)}$$

The protons are then tipped to an angle (α) away from alignment by applying an effective magnetic field (B_1^+) perpendicular to the main magnetic field to the sample via an excitation coil. (31). While B_1^+ is applied, the protons rotate along the perpendicular axis at the Larmor frequency (ω_0) with a slightly different phase, which is dependent on their spin-spin relaxation (T_2). After the B_1^+ pulse ends, protons return to their original alignment, based on their spin-lattice relaxation (T_1), and emit an RF signal, which can be detected using an RF receive coil. The RF signal transmission and reception processes are shown in Figure I-2, respectively.
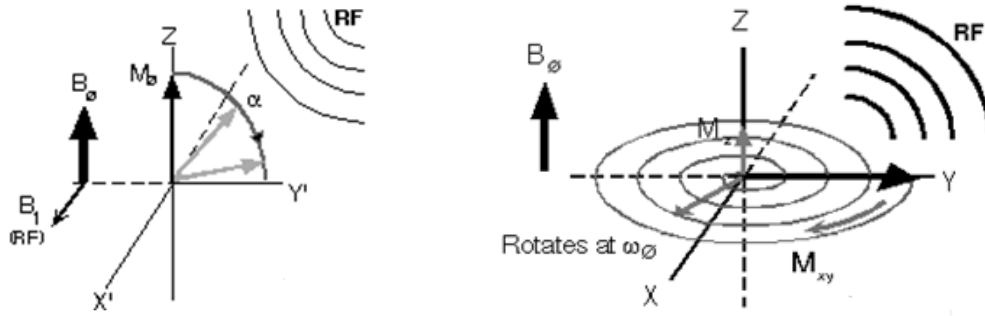
Figure I-2. Application of an RF pulse on a single proton. Applying an RF pulse (B$_1$) causes the proton to be tipped by an angle (α) away from its original orientation (left). When the pulse has ended, the proton relaxes back to its original orientation which emits a detectable RF signal (right). Reprinted with permission from (31).

I.1.2 RF Coils Background

As described, RF coils are a crucial part of an MR system because they are responsible for both transmission and detection of RF signals during MR experiments. In a standard clinical setup, as shown in Figure I-3, a single large RF coil is housed within the casing of the magnet bore and is often used for transmission and sometimes reception of the RF signal. However, this is not the case for every MR experiment, and local transmit and/or receive RF coils are sometimes placed within close proximity to a specific region-of-interest (ROI) and used for transmission and/or reception instead. These close-fitting coils lead to increased efficiency and sensitivity in comparison to the larger body coil (32,33).

MRI Scanner Components
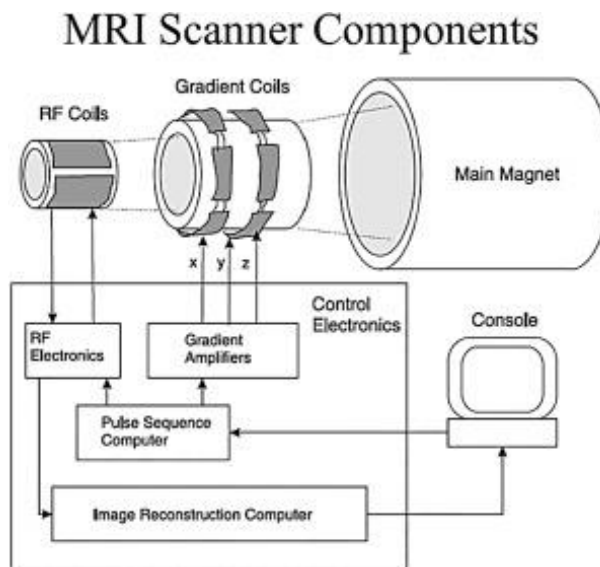
Figure I-3. Diagram of an MRI scanner set-up. The main magnet produces the external magnetic field, B_0. The gradient coils encode MR images providing localization information in the x, y, and z directions. Lastly, the RF coils are used to tip the protons out of alignment as well as detect the emitted signals. Reprinted from (34).

Since the initial experiments of Hoult and Lauterbur, it has been understood that the achievable signal in an MR experiment is dependent on a few factors: strength of the main magnetic field, gyromagnetic ratio of the nuclei, imaging parameters, efficiency of the RF coils, and dielectric and conductive losses of the sample being imaged (35). Therefore, this dissertation focuses on optimizing the achievable RF signal by using high magnetic fields (shown in Chapter 2) and closely-fitting RF coils (shown in Chapter 2 and Chapter 3).

Based on the principle of reciprocity, the signal-to-noise ratio (SNR) can be used to assess an RF coil for both its efficiency during transmit and sensitivity during receive

(35,36). Specifically, SNR can be measured using Eq I.2 (33). In Eq I.2, ω_0 is the Larmor frequency of the NMR-active nuclei in rad/sec (shown in Eq I.1), ΔV is the voxel volume, M_0 is the net magnetization, B_1^+ is the circularly polarized effective transmit magnetic field, k is Boltzmann's constant, T is the absolute temperature in Kelvin, Δf is the bandwidth of the receiver, and R_{coil} is the real part of the coil impedance.

$$SNR = \frac{\sqrt{2}\,\omega_0 \Delta V M_0 B_1^+}{\sqrt{4kT_c \Delta f R_{coil}}} \qquad \text{(Eq I.2)}$$

Assuming the sample, imaging parameters, and coil temperature remained the same, the SNR equation can be simplified to show that the SNR attributed to the coil (SNR_{coil}) as a function of the effective transverse magnetic field (B_1^+) and the resistance of the coil (R_{coil}), as shown in Eq I.3 (33).

$$SNR_{coil} = \frac{\sqrt{2}\,B_1^+}{\sqrt{R_{coil}}} \qquad \text{(Eq I.3)}$$

Various factors contribute to coil resistance such as: coil size, resistive and dielectric losses in components, quality of solder joints, and wire gauge, and these can all affect the SNR. Although some of these SNR losses are inevitable, constructing custom RF coils enables the flexibility to select designs and components which will

improve achievable RF signal for a specific study. Improvement of SNR, mostly via RF coils, will be covered in depth in later chapters.

I.2 Specific Aims and Dissertation Organization

The purpose of this work is to enable further studies of disease, in this case breast cancer and DMD, via construction of custom RF coils and additional hardware. Specifically, this work focuses on ^{1}H breast imaging at high magnetic fields, as well as ^{1}H and X-nuclei imaging and spectroscopy of formalin-fixed rectus femoris muscles as described in the aims below:

- Aim 1: Construction and evaluation of a 32-channel ^{1}H bilateral breast array for 7T. Upon completion, the coil was tested at UT Southwestern (UTSW) for its abilities to acquire images with high spatial and/or temporal resolution. A modified ^{1}H transmit volume coil using forced current excitation (FCE), constructed by collaborator Dr. Jiaming Cui (37), was used to assess the benefits of using an array coil in comparison to a volume coil.

- Aim 2: Construction of two double-tuned (^{1}H/^{23}Na and ^{1}H/^{31}P) birdcage coils for magnetic resonance imaging and spectroscopy of formalin-fixed GRMD rectus femoris muscles. Upon completion, the coils were first tested on phantoms which mimicked skeletal muscle tissue properties. Following phantom studies, ^{1}H T1-weighted and T2-weighted images, ^{23}Na images, and ^{31}P spectra were acquired on seven formalin fixed rectus femoris samples from various GRMD animal models.

- Aim 3: Biomarker analysis in rectus femoris GRMD tissue samples. Based on the data acquired in Aim 2, images and spectra were evaluated for changes corresponding to age (disease progression) of the sample. Various previously-reported biomarkers pertaining to ^{1}H imaging, ^{23}Na imaging, and ^{31}P spectroscopy were assessed.

Chapter 1 of this dissertation includes a description of NMR phenomenon and RF coils to emphasize the importance of custom hardware, specifically RF coils, in an MR experiment. Additionally, RF coils which were constructed to enable studies of the human breast and GRMD muscle samples are mentioned. The significance of using MRI and MRS to study disease, specifically breast cancer and DMD, is covered in more detail at the beginning of the respective chapters.

Chapter 2 describes the construction and evaluation of a bilateral 32-channel receive array and forced current excitation (FCE) volume coil for breast imaging at 7T. Coil performance was evaluated on homogeneous canola oil phantoms using a Philips Achieva 7T system. Throughout this section, the benefits of using an array coil, in contrast to the bilateral volume coil in T/R mode, were highlighted. Specifically, SNR maps, g-factor maps, and high spatial and temporal resolution images were acquired to demonstrate the advantages of using the array coil. Furthermore, performance of the bilateral coil array was also compared to the previously reported 16- channel unilateral coil with a similar design (38).

Chapter 3 and Chapter 4 describe the construction, evaluation, and utilization of two double-tuned birdcage coils for assessment of NMR indices in the GRMD model of

9

DMD. While Chapter III mostly focuses on construction and evaluation of the birdcage coils, Chapter 4 focuses on the utilization of the birdcage coils to study rectus femoris muscle samples. Coil performance was initially evaluated on the bench and on a 4.7T Varian Inova scanner. Specifically, ^{1}H images, ^{23}Na images, and ^{31}P spectra of various homogeneous phantoms were acquired to demonstrate the homogeneity of the coils as well as feasibility of distinguishing between various concentrations of ^{23}Na of ^{31}P solutions via imaging and spectroscopy.

Chapter 4 describes the acquisition of images and spectra of formalin-fixed rectus femoris GRMD samples, as well as how previously reported NMR indices vary with age. This study was performed on seven rectus femoris muscle samples varying from 3 months to 30 months. The NMR indices mentioned in Chapter 4 called for the acquisition of: ^{1}H T1-weighted (T1w) and T2-weighted (T2w) images, ^{23}Na images, and ^{31}P spectra. Prior to acquiring images and spectra on all the samples, imaging parameters, such as echo time (TE) and repetition time (TR) were optimized based on the T1 and T2 of the tissue.

Lastly, Chapter 5 is a review on the findings presented in Chapters 2- 4, as well as potential future work. Details pertaining to potential changes to RF coil designs are described for both applications mentioned in previous chapters, as well as the design of a graphical user interface for future GRMD studies.

I.3 Dissertation Style

This dissertation is written in accordance to style guidelines set by *Magnetic Resonance in Medicine*; meaning it is in AMA (American Medical Association) format. Chapter 1 consists of an introduction to the dissertation, mostly focusing on a broad overview on the use of MRI and MRS to study breast cancer and DMD. Chapters 2- 4 cover specific studies performed to enable disease evaluation. These chapters follow a structured format which consist of the following sections: introduction, methods, results, and conclusions. Lastly, the final chapter is a brief overview of the findings from the studies performed as well as potential future directions.

CHAPTER II

A 32-CHANNEL RECEIVE ARRAY AND MODIFIED FORCED CURRENT

EXCITATION TRANSMIT COIL FOR BILATERAL BREAST IMAGING AT 7T[1]

II.1 Synopsis

This work describes the construction and evaluation of a bilateral 32-channel

receive array and a forced current excitation (FCE) volume coil for breast imaging at 7T.

The volume coil was composed of two quadrature volume coils (one for each breast)

consisting of a saddle pair and a Helmholtz coil. The receive array consisted of 32

receive coils, placed on two 3D printed hemispherical formers. Each side of the receive

array consisted of 16 receive coils and corresponding detachable boards with match/tune

capacitors, active detuning circuitry, and a balun. Coil performance was evaluated on

homogeneous canola oil phantoms using a Philips Achieva 7T system. The performance

of the array coil was evaluated by comparison to the bilateral FCE volume coil in

transmit/receive mode and to a previously reported 16- channel unilateral coil with a

similar design. The array had an increase in average SNR throughout both phantoms by

a factor of five as compared to the volume coil, with SNR increases up to 10 times

observed along the phantom periphery. Noise measurements showed low inter-element

noise correlation (average: 5.4%; maximum: 16.8%). G-factor maps were acquired for

various acceleration factors and showed mean g-factors < 1.2, for acceleration factors of

up to six. Furthermore, the advantages of using the array were demonstrated by acquiring images with high temporal resolution (R=16, scan duration=10s), and accelerated images (R=4) with high spatial (0.75 mm isotropic) while remaining within comparable noise levels in comparison to the volume coil. The performance improvements achieved demonstrate the clear potential for use in dynamic contrast-enhanced or diffusion-weighted MR studies while maintaining diagnostically relevant spatial and temporal resolutions.

II.2 Introduction

In 2019, over 200,000 new cases of breast cancer were reported, making it the most commonly diagnosed cancer in the United States (3). Magnetic resonance imaging (MRI) of the breast is commonly used as a supplemental tool to mammography throughout various stages of disease management, from screening to surveillance of recurrence, because of its ability to detect breast cancers with high sensitivity (4-8,39). Furthermore, MRI techniques such as dynamic contrast-enhanced MRI (DCE-MRI) and diffusion weighted imaging (DWI) provide additional information about morphology and kinetics of breast lesions, which can enable the distinction between malignant and benign tumors with improved diagnostic accuracy (10-13). Several studies have reported the benefits of high field (7T) imaging in DCE and DWI studies (40-43), with the additional use of array coils particularly beneficial to increase the achievable temporal resolution (14,16-18,44,45).

The challenges of high field imaging with respect to homogeneous excitation and specific absorption rate (SAR) are well documented (46,47). Our group has previously

reported on the forced current excitation (FCE) technique to transmit effectively at 7T, achieving homogeneous excitation in the presence of the asymmetric loading associated with prone-patient breast imaging while easily remaining within SAR regulations (48). The insensitivity of the FCE approach to loading conditions was additionally demonstrated with the insertion of a 16-channel receive breast array designed for unilateral breast imaging (38). The approach is also beneficial for bilateral configurations because of its ability to provide homogeneous excitation throughout the region of interest (ROI) without the need for multiple transmit channels, its ability to mitigate effects of the mutual coupling between the left and right volume coils, and the potential for a switchable implementation (49,50).

This work describes the practical aspects of the design, construction and evaluation of a bilateral 32-channel receive array for imaging at 7T and an FCE transmit coil design modified to accommodate the array. The bilateral array provides the known advantages of simultaneous evaluation of both breasts for patients with contralateral lesions and providing a built-in control for cases in which lesions are confined to a single breast. Due to the lack of commercially available high channel count ^{1}H breast coils for 7T, the performance of the array coil was evaluated by comparison to the bilateral FCE volume coil in transmit/receive mode, as well as to the performance we previously reported on the 16- channel unilateral version of this coil (38). The coil was evaluated on homogeneous canola oil phantoms to assess its ability to achieve high temporal (by accelerating) and high spatial resolution imaging.

14

II.3 Methods

II.3.1 Transmit Volume Coil

A modified version of a previously-reported FCE bilateral breast coil was designed and constructed to allow space for the integration of the 32-channel receive array (50). The coil is composed of separate quadrature volume coils for each breast, each consisting of a saddle pair and a Helmholtz coil. The saddle pair consisted of two rectangular loop coils printed on flexible copper-clad FR-4 and conformed to the inside of a 3-D printed former with an inner diameter of 14.7cm. Concentric 3.5mm wide coplanar shields surrounded each loop to improve B_1^+ transmit efficiency at high fields (51). All four saddle elements were connected in parallel at a common voltage point (CVP) via $\lambda/4$ transmission lines to ensure equal currents through all elements, irrespective of loading (48). Shielded twinaxial cable (RG108, Pasternack) was used as the $\lambda/4$ transmission lines. The use of twinaxial cable avoided the usual balanced to unbalanced connection associated with using coaxial cable. This eliminated the need for integrated baluns and/or RF shields, as needed with previous bilateral FCE designs, making space for the receive coil array and all its corresponding hardware and cabling (38,48,49). A short twinaxial cable was used to connect the CVP to a match and tune board, which contained a variable matching and tuning capacitors (SGNMNC1206E, Sprague- Goodman) and a fixed matching capacitor (100C Series-7.2kV, ATC) to provide a semi-balanced match. Finally, a balun was integrated onto the coaxial cable

15

which connects the match/tune circuit to the transmitter to address the unbalanced-to-balanced transition. The match/tune circuitry for the Helmholtz pairs was identical to that of the saddle pairs, but joined at a separate common voltage point located on the other side of the structure. Each Helmholtz coil consisted of two concentric loops (i.d. 16.0 cm) approximately 8.0 cm apart with a surrounding 3.5mm wide concentric coplanar shield. The volume coil dimensions and simplified version of the FCE configuration are shown in Figure II-1. The FCE design also simplified the coil active detuning network due to the impedance transformation properties of the $\lambda/4$ transmission lines. The active detuning network consisted of a PIN diode (UM9415, Microsemi) in shunt at the CVP. By forward biasing the PIN diode during receive, a low impedance is presented at the CVP, which is transformed to a high impedance $\lambda/4$ away from the CVP at the coil feed-point to detune the coil. The biasing signal used for active detuning was generated by a single -5V DC signal split into separate lines for the saddle and Helmholtz coils. Bias tee networks provided isolation of the RF/DC paths where the signal was inserted at the coil CVP.
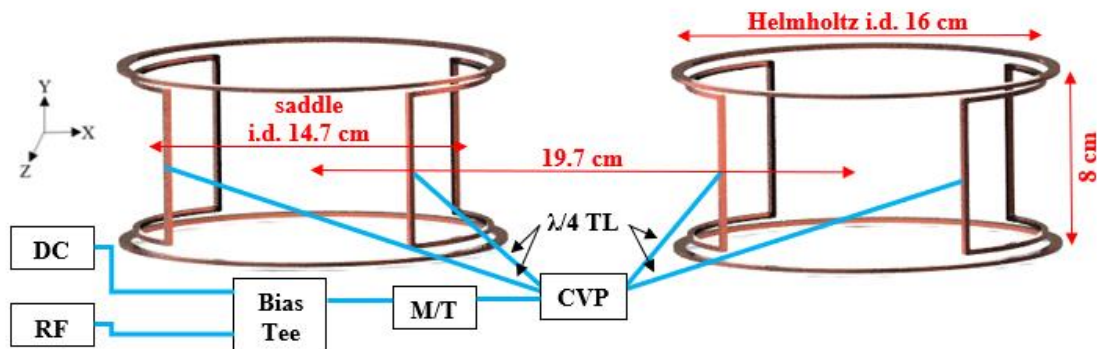
Figure II-1. Bilateral FCE transmit volume coil. The coil is composed of two quadrature volume coils, one saddle pair and Helmholtz coil on each side. The saddle elements (width 15.3 cm; length 8.1 cm) were mounted on a cylindrical former (i.d. 14.7 cm; aperture angle 120°). The Helmholtz elements (i.d. 16.0 cm) were placed 8 cm apart. All saddle elements, as well as all Helmholtz elements, were joined at a CVP with twin axial cable λ/4 away from the coil's feed-point (example configuration for the saddle coil shown in blue). A short cable length was then used to connect the match/tune to the CVP. For simplicity, CVP and match/tune circuitry for the Helmholtz elements and the co-planar shielding around each element of the coils are not shown.

II.3.2 Receive Coil Array

Size and placement of each element on the bilateral 32- channel receive array

was based on the design of the previously reported unilateral 16-channel receive array,

which used the "soccer-ball" configuration presented by Wiggins et al. (38,52). The coil

former for each breast was a hemispherical 3D-printed shell with a volume of 900 mL,

meaning it can accommodate approximately 80% of the general female population (53).

Extruded cuts on the outer surface of the shell, in the arrangement of the array, were

integrated into the design to hold each element and passive detuning trap in place. Each

hemispherical shell consisted of three rows of elements in the anterior/posterior

direction. The row closest to the chest wall had nine receive elements, the second row (moving toward the apex of the shell) had six receive elements, and the last row (at the apex) has one large receive element. The layout of the receive array, looking down from the apex, is shown Figure II-2.
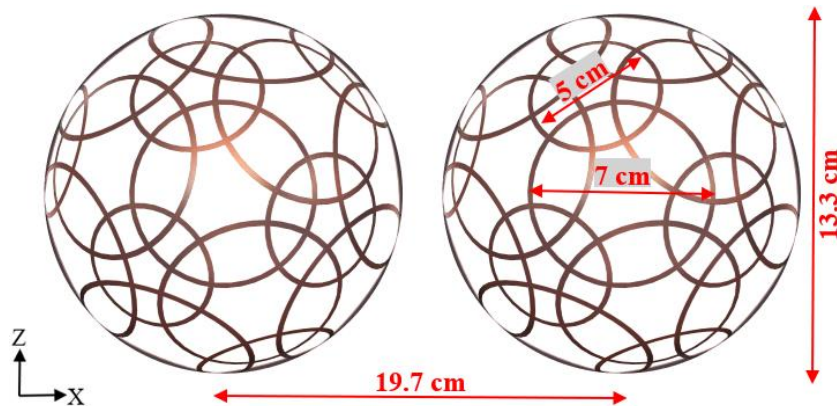
Figure II-2. Receive coil array layout. The bilateral receive array is shown, with each side containing 16 of 32 elements. The diameter of the array former is 13.3 cm and is made up of large (7 cm) and small (5 cm) elements. The elements are placed on the former following a "soccer-ball" pattern.

Individual elements of the array were printed on flexible (0.51 mm) copper-clad FR-4 in a "C"- shape, as described in By et al. (38). The edges of the printed coil were then brought together, allowing for the coil to conform and be placed within the extruded cuts of the 3-D printed coil former. Each receive element had six equally-spaced breaks: four breaks containing fixed capacitors (1111C series, Passive Plus), one break containing a passive detuning network, and another break containing a male SMA

connector which connected to a detachable board containing the match/tune/decoupling

network for each element. The passive detuning network was located opposite the

detachable board and consisted of two fast-switching crossed diodes (UM9989,

Microsemi), a fixed inductor (2508-27NJLB, Coil Craft), and a variable capacitor

(SGC3S100NM, Sprague-Goodman). A schematic of a single receive element is shown

in Figure II-3, with all component values and functions detailed in Table II-1.
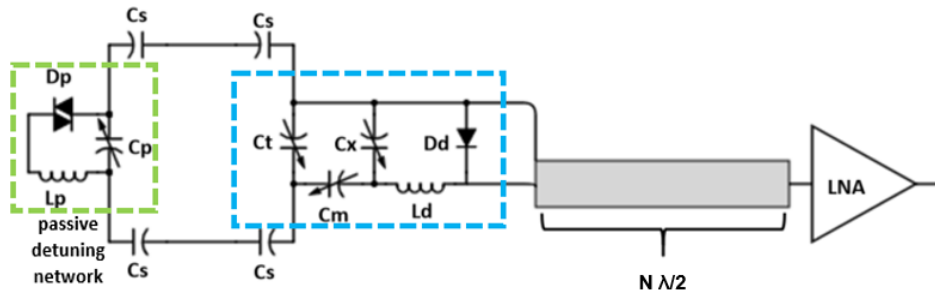
Figure II-3. Schematic of single receive element. Circuit schematic of a single receive element showing four segmented capacitors, a passive detuning network (in the green dashed box), and a matching network with active detuning integrated (in blue dashed box). Component names, descriptions, and values are shown in Table II-1.

Label	Description	Value
Cs	segmented capacitors	8.2 pF / 13pF
Lp	passive trap inductor	27 nH
Cp	passive trap capacitor	3- 10 pF
Dp	passive trap diodes	-
Ct	tuning capacitor	3- 10 pF
Cm	matching capacitor	3- 10 pF
Cx	active trap capacitor	3- 10 pF
Ld	active trap inductor	13 nH
Dd	active trap PIN diode	-

Table II-1. Components used in receive elements. Aside from the segmented capacitors (large element/small element), the same components were used for both small and large receive elements.

The detachable boards for each receive element allowed the array to be inserted into and removed from the close-fitting volume coil, as well as simplified initial tuning and troubleshooting of each element. These processes were simplified by disconnecting, or open-circuiting, all but one element at a time at its SMA connector, therefore enabling each element to be analyzed independently. The match/tune/decoupling networks were based on the design presented by Reykowski et al., which adds one degree of freedom by adding capacitor C_x (54). Specifically, this additional degree of freedom lends itself well to coils tuned at high operating frequencies, such as 298 MHz, because it allows the flexibility to choose component values that are not unreasonably small. The equations used for initial matching/tuning/decoupling of individual receive elements, are shown in Eq II-1 – Eq I-7; where Z_0 is 50Ω and X_{Amp} is 0Ω (54). The coil impedance (Z_L) of each

20

receive element was measured using a VNA (E5071C, Agilent Technologies) S_{11}

measurement in smith chart mode after performing a port-extension calibration. When

the S_{11} measurement was acquired, all the coils, including their segmenting capacitors

(C_s) and passive detuning traps, were also mounted on the 3D printed shell.

$$Z_L = (R_L + jX_L)\Omega \qquad \text{(Eq II.1)}$$

$$A = X_L Z_0 + R_L X_{Amp} \qquad \text{(Eq II.2)}$$

$$B = \sqrt{R_L Z_0 (X_{Amp}^2 + Z_0^2)} \qquad \text{(Eq II.3)}$$

$$C = R_L Z_0 - X_L X_{Amp} \qquad \text{(Eq II.4)}$$

$$X_{Ct} = \frac{X_{Cx} A}{X_{Cx} Z_0 - B} \qquad \text{(Eq II.5)}$$

$$X_{Cm} = X_{Cx} \frac{A - B}{B} \qquad \text{(Eq II.6)}$$

$$X_{Ld} = X_{Cx} \frac{A - B}{A} + Z_0 \frac{C}{A} \qquad \text{(Eq II.7)}$$

Variable capacitors (SGC3S100NM, Sprague-Goodman) were used for C_t, C_m,

and C_x in the network, as shown in Figure II-3. Additionally, a fixed inductor (2508-

27NJLB, Coil Craft) and a PIN diode (MA4P7470F-1072T, MACOM) were used for

active detuning. Custom-made can baluns were included after the network to suppress

common-mode currents. Each balun was constructed of semi-rigid cable twisted into a

solenoidal inductor resonated with a fixed capacitor (1111C series, Passive Plus). One

endcap of the can balun had a tapped hole, where a brass screw was inserted into. Adjustment of this screw, located at the core of the balun's solenoidal inductor, allowed for slight variation in the balun's inductance to aid in tuning. A flexible coaxial cable (7805-010, Belden) was directly soldered onto each detachable board, with a BNC connector (2-331350-4, TE Connectivity) on the opposite end for connection to the remote Philips 32 channel preamplifier interface box. The total phase (θ_{total}), including the phase from each balun (θ_{balun}) and the phase from cabling within the interface box ($\theta_{interface}$), was measured to be an integer half-wavelength multiple at 298 MHz to ensure that the decoupling preamplifier presented a low input impedance at the coil decoupling network, as shown in Eq II.8. The phase angle of the interface box ($\theta_{interface}$) was calculated based on the measured impedance of four channels in the 32-channel interface box. Impedance measurements were taken using a VNA in smith chart mode when the preamplifiers were powered. Specifically, this was done by connecting the interface box to the scanner via its ODU connector, then directly connecting a RG58 transmission line, after a port-extension calibration, from the VNA to the BNC connector on the interface box. This measurement was taken 25 times over four different channels. The average input impedance was then used to construct a mock preamplifier box to measure preamp decoupling of individual receive elements.

$$\theta_{total} = N\frac{\lambda}{2} = \theta_{balun} + \theta_{cable} + \theta_{interface} \qquad \text{(Eq II.8)}$$

In this case, the coaxial cable length required to reach the interface box and achieve the appropriate decoupling requirement was approximately 113cm, corresponding to a total length from the coils to the preamplifiers of four half-wavelengths. Cables were bundled together with a cable sleeve and tuned, two floating cable traps (55) were added on each bundle along its length.

II.3.3 Testing/Troubleshooting Hardware

Additional hardware, including a mock preamplifier box, DC fan-out board, bias tees, and a PIN diode driver were all constructed to test the array coil on the bench and while imaging. Specifically, a 16-channel mock preamplifier box was used to test the preamp decoupling of the receive elements by mimicking the phase presented at the BNC connector of the Philips interface box (56). It was constructed of two transmission lines for each channel, one for signal and one for ground, milled on a copper-clad FR4 board. The two transmission lines had a PCB-mount BNC connector on one end and a 0.5Ω resistor in shunt on the distal end. The phase of each channel in the mock preamplifier box was measured in a similar manner to that of the Philips interface box. Based on the phase measured, the resistor was moved along the transmission lines until the desired phase, or average phase in the Philips interface box, was achieved (~87°).

A 32-channel fan-out board was constructed to test the active detuning of all receive elements on the bench and during the troubleshooting process. Since the fan-out board was intended to be used within the bore of the 7T scanner during the troubleshooting process, the frame of was constructed of acrylic. Overall, the fan-out board consisted of two milled copper-clad FR4 boards with a single DC input for each

PCB board (which was connected to a variable power supply) and 32 total outputs. Each line on the fan-out board consisted of an RF choke, a 50Ω current-limiting resistor (WFMA Series, Vishay), an 1800 pF decoupling capacitor (1111C Series, Passive Plus), and a short coaxial cable with a BNC connector. The BNC connectors, from the board output, were then connected to the auto-terminating BNC adapters (BA307, L-com) on the acrylic frame. The fan-out board supplied a -5V, 100mA forward-biasing signal to the active detuning PIN diodes on all 32 receive elements.

Additionally, a PIN diode driver and 32 external bias tees were constructed after observing inhomogeneities in B_1^+ maps and T/R volume coil images. Specifically, since these inhomogeneities had not appeared in previous tests and were mostly confined to one side of the bilateral, it was believed that this occurred because of improper active detuning of one or more receive elements during transmit. Therefore, a PIN diode driver (57) and external bias tees were built to provide a -5V, 100mA forward-biasing, and a +12V reverse-biasing signal to the receive elements during transmit and receive, respectively.

II.3.4 Bench Measurements

Elements were initially matched and tuned individually using a VNA S_{11} measurement with all 16 coils already mounted on the 3D printed hemispherical shell. To simplify the tuning process, all additional elements were detached from their match and tune boards (or open-circuited). S_{12} measurements, using a double-loop probe, were taken to measure the active detuning of each receive element. Active detuning was measured in standard fashion, by taking the difference in the S_{12} measurements (at 298

MHz) when the receive element was terminated with a 50Ω load and again when the

active detuning PIN diode was forward-biased by the signal from the fan-out board.

Finally, the preamplifier decoupling of each coil was measured in the same manner as

the active detuning except, instead of forward-biasing the PIN diode, the mock

preamplifier box was used, as shown in Figure II-4.
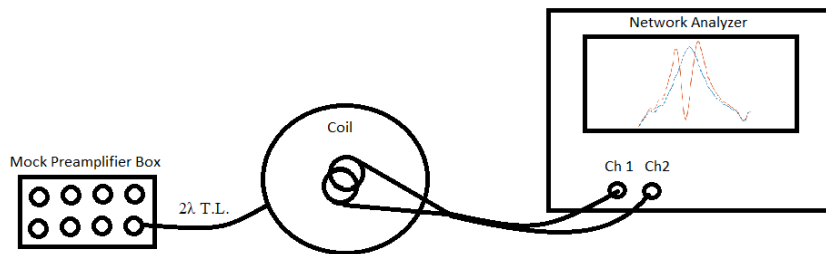
Figure II-4. S_{12} preamplifier decoupling measurement setup. This double-loop probe setup is used to measure the trapping resonance of a coil when connected to a mock preamplifier box. As described, this measurement was performed in the same manner as the active detuning.

After initial matching/tuning/active detuning of all receive elements, the

detachable boards were removed and the receive array was placed into the volume coil.

The detachable boards were then attached to their corresponding receive elements four at

a time while inside the volume coil. S_{11} and S_{12} measurements were then repeated on

each coil with all receive elements (except for the one being measured) and the volume

coil actively detuned. This process was repeated until all 32 channels were matched, tuned, and actively detuned.

II.3.5 Imaging

All scanner data were acquired on a Philips Achieva 7T system. Two homogeneous canola oil phantoms encased in watertight 3D printed hemispherical shells were used to mimic the lipid properties of the breast (58). Various images were acquired throughout the construction and troubleshooting processes. However, for brevity, only the final images acquired are covered in this chapter, while the remaining images (acquired throughout the troubleshooting process) are detailed in Appendix A.

B_1^+ maps were first generated using a [3D T1-weighted fast field echo (T1FFE)] pulse sequence with the actively detuned receive array in place. Images to demonstrate the SNR gains achievable with the array were obtained using the following acquisition parameters: 3D T1-weighted turbo field echo pulse sequence (T1TFE) without fat suppression, TE: 1.77 ms, TR: 5 ms, FOV: 152 x 131 x 352 mm^3 (AP x FH x RL), resolution: 1mm isotropic, and scan duration: 161s. Images were acquired using the volume coil in T/R mode, with the receive array kept in place, and using the 32-channel array to receive and the volume coil in transmit-only mode. Noise-only datasets were also acquired for both configurations using identical imaging parameters but with the transmit pulse disabled.

The potential benefit provided by the SNR gains were demonstrated via g-factor mapping and the acquisition of high spatial and temporal resolution imaging within the bounds of maintaining a clinically relevant scan time (~90 s) and image quality

comparable to the volume coil. Geometry factor (g-factor) maps were acquired using the same imaging parameters as detailed above with SENSE acceleration factors of 1x, 2x, or 3x in the foot-to-head (F/H) and/or 1x, 2x, or 3x in the left-to-right directions (L/R). To demonstrate the potential high temporal resolution enabled by the array, the 1mm isotropic resolution was kept the same and the acceleration factor was increased to the point of maintaining the image quality achieved by the volume coil (an acceleration factor of R=16; scan time 10s at the limit). Lastly, to demonstrate the potential high spatial resolution enabled by the array, the acceleration factor and resolution were adjusted to stay within the bounds of a scan time of 90 seconds and maintaining image quality comparable to the volume coil (R=4; 0.75mm iso at the limit).

II.3.6 Data Analysis

Image processing and analysis were performed using in-house Matlab scripts on reconstructed images exported from the Philips system. B_1^+ maps were masked manually to include the entire region of the phantom, and a profile through the center of the phantom was plotted to evaluate B_1^+ homogeneity (with the detuned array in place). The B_1^+ homogeneity was measured in standard fashion, by taking the standard deviation over the ROI and dividing it by the mean of the same region, in this case throughout the phantoms on both sides of the bilateral coil (14,18). SNR comparisons between the array and the volume coil were performed on an axial slice at the center of the phantoms by taking the average and maximum signal value throughout both phantoms and dividing it by the standard deviation of the noise in the noise-only image then scaling by a factor of 0.655 (59). An SNR map was generated for each image by dividing the signal intensity

by the standard deviation of a selected region in the noise-only image on a pixel-by-pixel basis. Finally, to show the SNR improvements of the coil array, an SNR map comparison was made by simply dividing the SNR map of the array by the SNR map of the volume coil. As with the B_1^+ map, SNR and SNR comparison maps were masked manually during post-processing in Matlab, and profiles along a centerline in the phantom were taken for evaluation and quantification.

To assess coupling between receive elements, a 32x32 noise-correlation matrix was generated by computing correlation coefficients between all combinations of images reconstructed from the noise-only datasets from each array element. Average, minimum, and maximum noise-correlation was evaluated on receive channels 1-16 and 17-32 separately since the two sides had negligible coupling with each other. The maximum and average g-factors were calculated within the masked region for all g-factor maps. The images at the limits of the high spatial and temporal resolution parameters detailed above were qualitatively and quantifiably compared by examining a small region within the center of the phantom, where the g-factor was highest. Quantification was made by taking the ratio of the mean of the signal in this region to the standard deviation in the same region after applying a high-pass filter to eliminate the signal variations due to coil patterns. Because acceleration was involved, this measurement does not directly correlate to signal-to-noise comparisons, but rather what we are referring to as image quality in this case.

II.4 Results and Discussion

II.4.1 Array Coil and Testing/Troubleshooting Hardware

Side and front views of the bilateral 32- channel array inside the transmit coil are shown in Figure II-5A and Figure II-5B, respectively. The ergonomic construction of this coil, including the 3D-printed top cover, the cushioned edges, and the rounded corners were all intended to maximize patient comfort. An acrylic platform, shown at the bottom of Figure II-5B, was placed over the coaxial cables to prevent the raised arms of the prone patient from coming in contact with them.
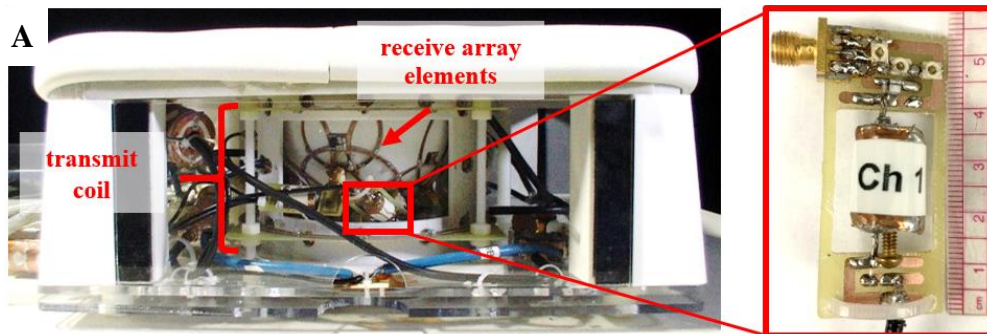
Figure II-5. 32-channel receive array in volume coil. A) Side view, receive array within the volume coil with the inset showing an example of the detachable match/tune/decouple boards. B) Top view of the coil and acrylic platform where the patient will be resting her head and arms.

B
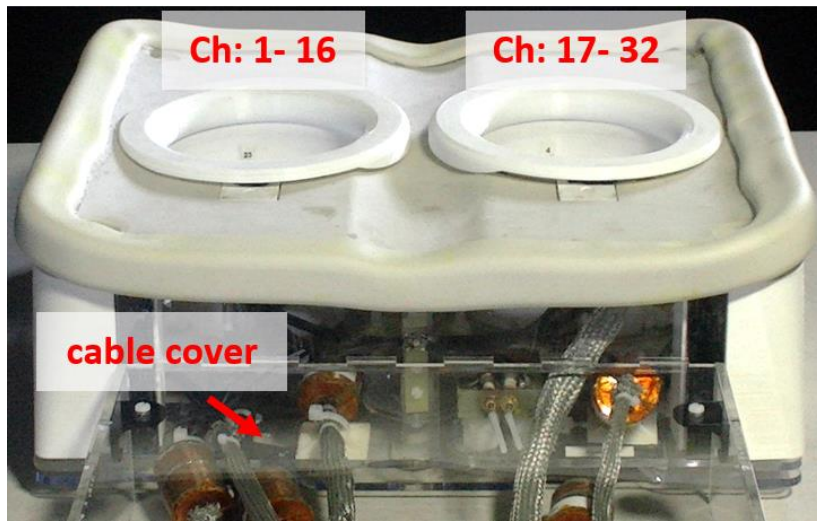
Figure II-5 Continued.

Eight channels of the 16-channel mock preamp box are shown in Figure II-6. This mock preamp box was constructed to mimic the average phase calculated from the impedance measurement of four channels in the Philips interface box (~87°). Therefore, the average phase for all 16 channels was 89.4°± 0.7°.

Figure II-6. 16-channel mock preamplifier box. Eight of the 16 channels of the mock preamp box are shown including the transmission lines, 0.5Ω resistors in shunt, and BNC panel-mount connectors.

The 32-channel fan-out board used to actively detune receive elements is shown in Figure II-7. The construction, including the acrylic frame and the stacked layout of the 32 channels, were done to allow the insertion of the fan-out board into the bore of the 7T scanner while troubleshooting. Each PCB of the fan-out board, shown in inset, is used to split a single input into 16 forward-biasing signals (-5V,100mA) to actively detune the receive elements.
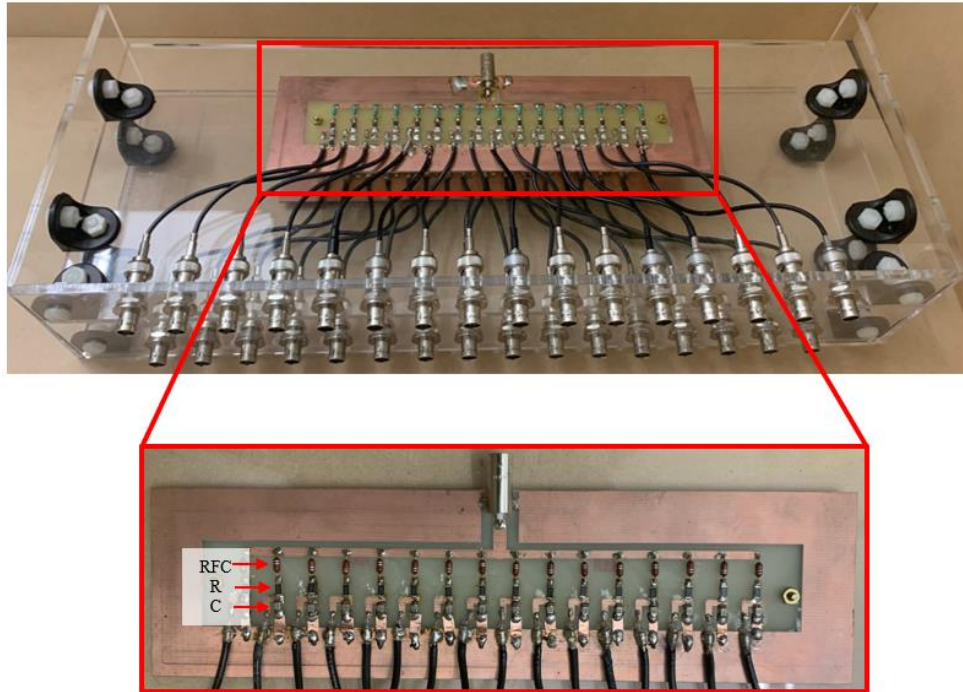
Figure II-7. 32-channel fan-out board. The complete fan-out board consist of two PCBs, as shown in the inset, mounted on two separate acrylic panels. Each PCB has a single BNC input (shown on the top end) and 16 outputs (coaxial cables). Additionally, each line of the fan-out board contains an RF choke (RFC), a current-limiting resistor (R), and decoupling capacitor (C).

A PIN diode driver and 32 external bias tees were constructed after observing inhomogeneities in B_1^+ maps and T/R volume coil images. The PIN diode driver, shown in Figure II-8A, provided a voltage of -5V,100mA to actively detune the receive elements, or a voltage of +12V to tune the receive elements. The driver output voltages were controlled by the input TTL signal from the Philips system. The output voltage from the PIN diode driver was split into two ports with each output port providing either -5V or +12V to 16 receive elements. These output ports were then connected to the "DC

Ports" on the bias tees shown in Figure II-8B. Lastly, the receive elements were connected to the "Coil Ports" of the bias tees, while the coaxial cables on the distal part of the box (or the "Philips Interface Ports") were connected to the 32-channel Philips interface box. This setup allowed for the comparison of actively detuning the receive elements via the custom PIN diode driver as opposed to the Philips interface box, as mentioned in Appendix A.
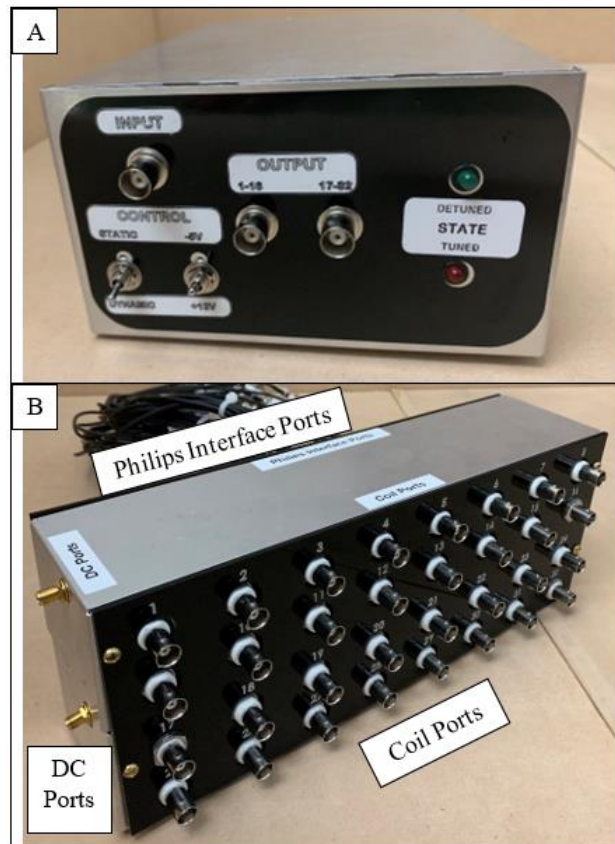
Figure II-8. PIN diode driver and bias tees for external active detuning. The PIN diode driver (top) is used to provide a DC voltage through the "DC Ports" to the bias tees (bottom) in order to actively detune or tune receive elements during transmit or receive, respectively.

II.4.2 Bench Measurements

The S_{11} measurements showed an average of -24 dB (min: -15dB; max: -40 dB)

of matching and tuning for all coils. The S_{12} double-loop probe measurements showed

an average of 23 dB (min: 17dB; max: 26dB) active detuning, and an average of 12 dB

(min: 10dB; max: 15dB) preamplifier decoupling. Additionally, the average Q was 71

for all the small elements and 47 for all the large elements. The two lowest Q values of 9

and 20 correspond to the two large elements located at the apex. Due to the location of these two elements, their low Q values can be attributed to the close proximity of the copper from the surrounding coils and their detectable boards, as well as the concentric placement of the elements relative to the bottom Helmholtz loop. All the bench measurements acquired on each coil are shown in Table II-2. Overall, the measurements indicated appropriate matching and tuning, active detuning, and preamp decoupling of all the receive elements.

	S_{11} [dB]		S_{12} [dB]		
Coil #	Matching/Tuning	Coil Q	Active Detuning	Passive Detuning	Preamp Decoupling
1	-23.3723	56.3063	24.9908	27.7	11.2
2	-19.6884	41.9486	22.479	21	12.5
3	-17.8596	54.3667	25.3544	23.9	**15.4**
4	-21.1302	85.237	26.0711	27.8	10.8
5	-34.6926	38.9068	25.2162	21.4	11.7
6	-35.5065	47.3937	23.9484	25.7	12.8
7	-20.1151	50.2725	22.8247	25.4	10.2
8	-27.8073	49.8757	24.1877	22.4	11.1
9	-17.763	40.6098	22.6264	24	11.5
10	**-40.6564**	72.1093	25.339	21.3	12.6
11	-21.1159	83.1461	24.601	27	**9.8**
12	-23.6082	43.1563	24.2002	24.6	12.1
13	-24.3913	72.3385	24.8407	28.3	11.5

Table II-2. Bench measurements for individual receive coil elements. The minimum and maximum values of each measurement are shown in bold and underlined in their corresponding columns. Overall, S_{11} and S_{12} measurements showed good coil performance of individual receive elements, with the exception of the low Q values from the two coils located at the apex.

Coil #	S_{11} [dB]		S_{12} [dB]		
	Matching/Tuning	Coil Q	Active Detuning	Passive Detuning	Preamp Decoupling
14	-20.867	42.0765	23.5572	21.4	13.8
15	-30.2156	72.8199	**26.2216**	22.6	13.4
16	-19.7321	**9.0954**	21.9488	20.8	13.1
17	**-15.4903**	62.9116	23.2377	30.9	10.56
18	-21.9268	51.3804	25.0655	**19.6**	13.4
19	-18.8798	70.5792	24.2293	22.9	12.5
20	-25.0552	69.2667	25.3272	22.4	12.9
21	-20.0223	40.5364	22.7285	23	11.8
22	-23.4307	58.1171	20.4001	23	13.1
23	-23.6022	**89.9587**	23.812	27.2	11.4
24	-36.7347	61.7652	25.0705	29	14.1
25	-18.9733	36.2266	19.1682	30	12.4
26	-27.2866	69.3266	20.7657	25	11.8
27	-26.7092	78.6633	22.7688	**36.2**	13.1
28	-36.6411	51.7875	19.8259	20.6	12.4
29	-25.5913	58.3692	23.1156	25.9	10.8
30	-20.112	40.5246	21.9433	25	10.7
31	-15.5686	79.3326	23.5349	27.7	11.1
32	-22.7265	20.8302	**16.9946**	23	12.8

Table II-2 Continued.

II.4.3 B_1^+ Measurements and SNR Measurements

The acquired B_1^+ map shows similar profiles on both bilateral sides, with more signal being produced on the left side and a more homogeneous region towards the center of each phantom, as seen in Figure II-9. As shown in the profile there is a slight decrease in signal on the right phantom compared to the left which was potentially related to the location of the coil feed points. The coefficient of variation (standard

deviation/mean) showed a B_1^+ homogeneity of 17% throughout both phantoms for this slice, comparable to other previously presented breast coils tailored for transmission at 7T (14,18).
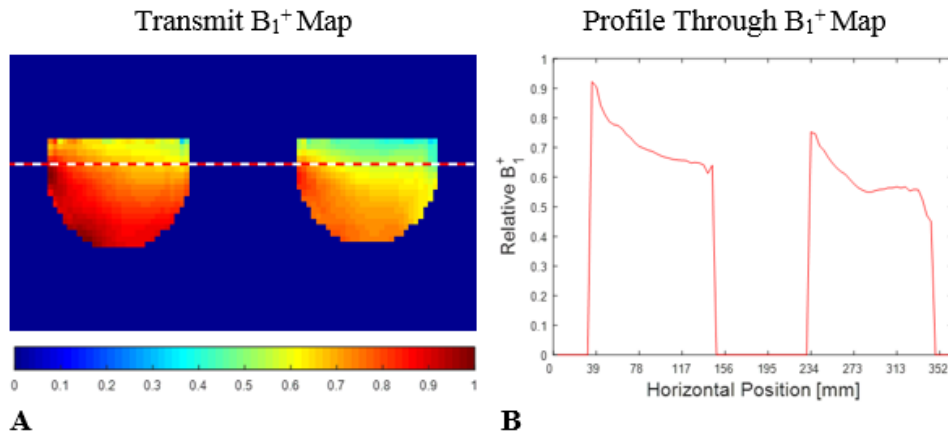
Figure II-9. B_1^+ map and profile through center of canola oil phantom. A) Bilateral B_1^+ map of homogeneous canola oil phantom. The mean of the relative B_1^+ of the left phantom is 87.2, while the mean of the right phantom is 72.5, or a difference of about 17%. B) A profile along centerline (indicated by red line in (A)) shows that more B_1^+ field is being produced on the left side of both phantoms, with a variation of 30% and 27% on the left and right phantom, respectively.

SNR measurements show an average SNR of 16 for the volume coil, and an average SNR of 79 for the array coil over the entire phantom. The SNR maps for the two coil configurations are shown in Figure II-10A-B. The SNR map for the volume coil is relatively homogenous throughout both phantoms, while the SNR map for the receive array shows a larger increase in SNR along the periphery and drops off as we move

towards the center of the phantom as expected. The comparative SNR map (array coil divided by volume coil), shown in Figure II-10C, indicates the increase in SNR for the array coil throughout the entire phantom, even at the center. Specifically, profiles taken along a centerline (location in red on each SNR map) indicated an increase of approximately three times in the center and ten times along the periphery, as shown in Figure II-10D. The SNR comparisons between the array and volume coil in the bilateral configuration are slightly higher than our previously reported 16-channel unilateral version, which had a mean improvement of 3.3 times throughout the phantom and 2.1 times in the center (38). This difference is most likely due to loading and shielding effects from the presences of the (detuned) array during volume coil imaging in this study. When acquiring volume coil data in the 16-channel unilateral case, the volume coil could be matched and tuned within the range of the variable capacitors with the array completely removed, leading to a higher volume coil SNR and therefore a slightly less favorable comparison relative to the bilateral configuration.
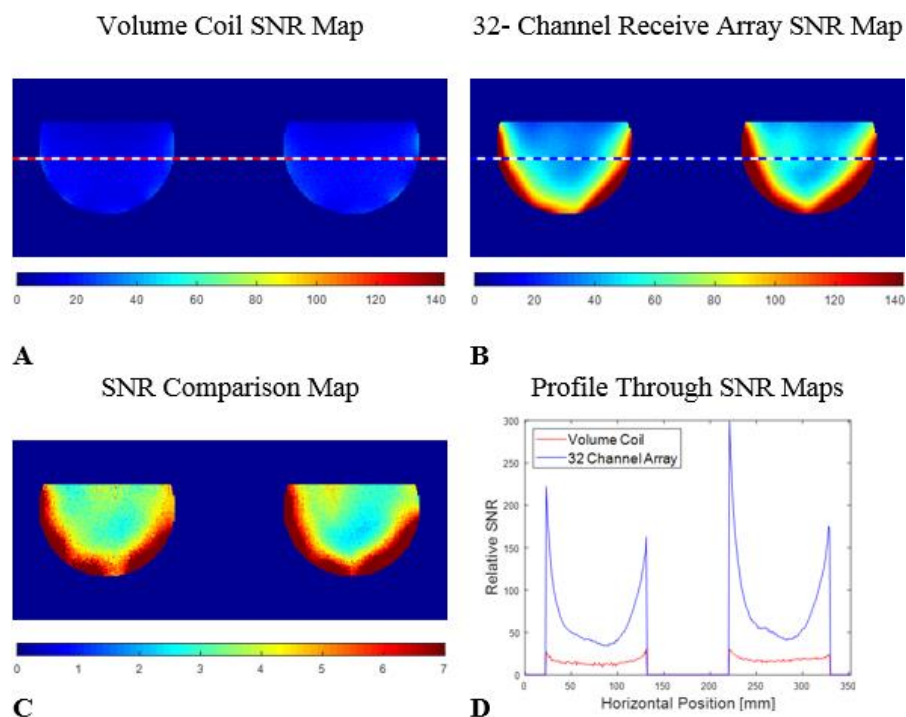
Figure II-10. SNR maps and profiles through maps using the volume coil in T/R mode and the 32-channel receive array. A) SNR map of the volume coil in T/R mode showed an average SNR of 16 throughout the phantom and an average SNR of 14 in the center. B) SNR map of 32- channel receive array showed an average SNR of 79 throughout the phantom and an average SNR of 42 in the center. C) SNR comparison map (32-channel receive array SNR map / volume coil SNR map) showed an increase in SNR throughout the entire phantom with larger increases toward the periphery. D) Profile along the center of the phantom (shown by red line) show an increase in SNR of about three times at the center and an increase of up to ten times along the periphery.

II.4.4 Individual Coil Images and Noise-Correlation Measurements

Images from individual coil elements were reconstructed on the Philips system.

Each of these image datasets contained two dynamics, one corresponding to the signal

and the other to the noise, for each coil. Due to the spatially dependent coil sensitivity

patterns, images were displayed over three different planes, as shown in Figure II-11A. Additionally, Figure II-11B the placement of each receive element on the 3D printed shells.
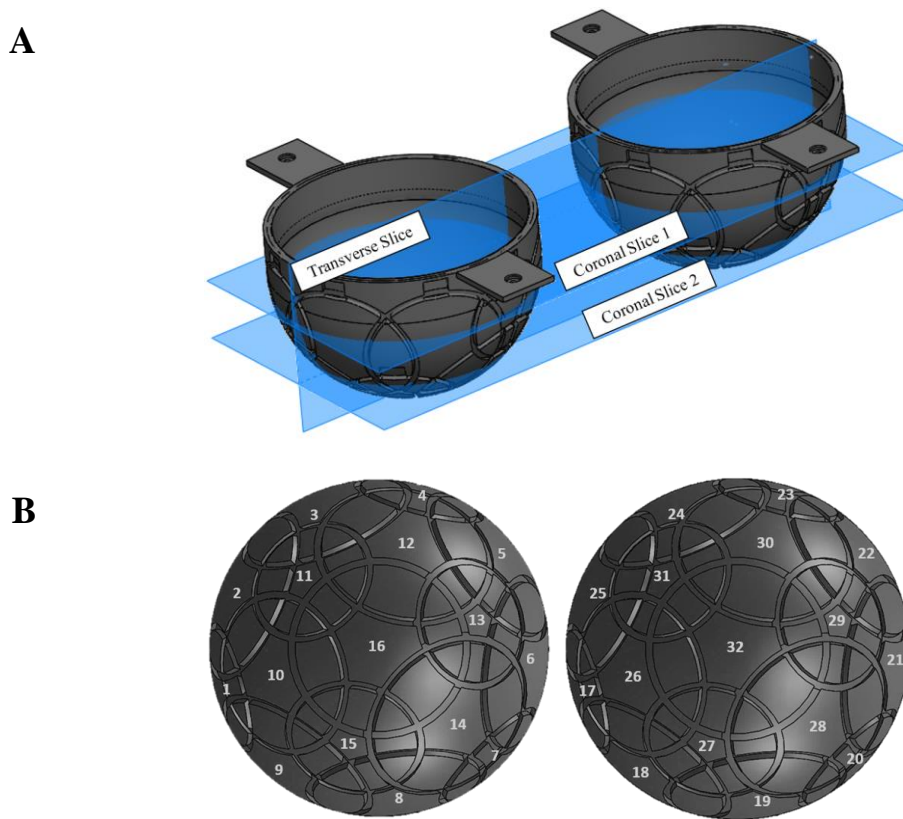
Figure II-11. Slice selection and coil placement references for individual coil images. A) Coronal Slice 1 was used to display the images from the coils closest to the chest wall (coils: 1-9 and 17-25). Coronal Slice 2 was used to display the images from the coils in the second row, moving toward the apex of the shell (coils: 10-15 and 26-31). Lastly, Transverse Slice was used to display images from the coils located at the apex (coils: 16 and 32). B) Individual coil placement on the hemispherical shells show that coils 1-16 were placed in a clockwise pattern, while coils 17-32 were placed in a counter-clockwise pattern.

Individual coil images were displayed on the same scale to show the relative sensitivity patterns of each receive element. As shown in Figure II-12, the sensitivity patterns corresponding to coils 1-16 appear more localized than those of coils 17-32. However, it is still apparent that coils 1-16 were placed in a clockwise pattern, while coils 17-32 were placed in a counter-clockwise pattern on their 3D printed formers. Additionally, coil 25 showed a maximum signal approximately an order of magnitude lower than the rest of the receive elements, despite the comparable bench measurements. This decrease in sensitivity (also seen in previous tests) can possibly be attributed to changes in the coil during transportation or coil interactions under high power.
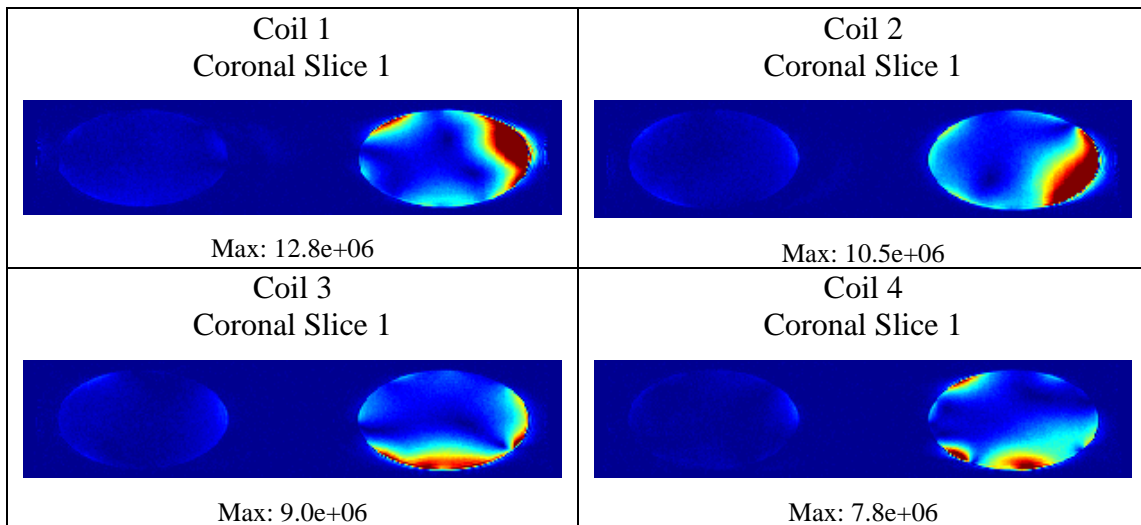
Figure II-12. Individual coil images. Three different slices were chosen, as shown in Figure II-11A, based on the location of the coils. Images from coils 1-16 correspond to the coils placed clockwise on the right hemispherical shell, while images from coils 17-32 correspond to the coils placed counter-clockwise on the left hemispherical shell, as shown in Figure II-11B.

Coil 5 Coronal Slice 1	Coil 6 Coronal Slice 1
Max: 4.4e+06	Max: 6.0e+06
Coil 7 Coronal Slice 1	Coil 8 Coronal Slice 1
Max: 6.0e+06	Max: 3.8e+06
Coil 9 Coronal Slice 1	Coil 10 Coronal Slice 2
Max: 6.4e+06	Max: 10.3e+06
Coil 11 Coronal Slice 2	Coil 12 Coronal Slice 2
Max: 12.8e+06	Max: 8.9e+06
Coil 13 Coronal Slice 2	Coil 14 Coronal Slice 2
Max: 13.5e+06	Max: 6.3e+06

Figure II-12 Continued.

Coil 15 Coronal Slice 2 Max: 11.2e+06	Coil 16 Transverse Slice Max: 8.3e+06
Coil 17 Coronal Slice 1 Max: 11.2e+06	Coil 18 Coronal Slice 1 Max: 8.8e+06
Coil 19 Coronal Slice 1 Max: 5.2e+06	Coil 20 Coronal Slice 1 Max: 5.8e+06
Coil 21 Coronal Slice 1 Max: 6.5e+06	Coil 22 Coronal Slice 1 Max: 5.2e+06
Coil 23 Coronal Slice 1 Max: 8.4e+06	Coil 24 Coronal Slice 1 Max: 8.0e+06

Figure II-12 Continued.

Coil 25 Coronal Slice 1	Coil 26 Coronal Slice 2
Max: 7.1e+05	Max: 12.0e+06
Coil 27 Coronal Slice 2	Coil 28 Coronal Slice 2
Max: 11.7e+06	Max: 9.3e+06
Coil 29 Coronal Slice 2	Coil 30 Coronal Slice 2
Max: 12.9e+06	Max: 8.1e+06
Coil 31 Coronal Slice 2	Coil 32 Transverse Slice
Max: 11.0e+06	Max: 6.5e+06

Figure II-12 Continued.

The noise-correlation matrix, based on the noise-only images from individual receive elements, shows a mean noise-correlation of 5.7% and maximum noise-correlation of 16.5% for coils 1-16, and a mean noise-correlation of 5.0% and a

maximum noise correlation of 16.8% for coils 17-32. Noise-correlation is minimal (less than 3.1%) between coils on the left breast side (receive elements 1-16) and coils on the right breast side (receive elements17-32), as shown in Figure II-13. In this case as well, the bilateral array performed similarly to the unilateral version which had mean noise-correlation of 6.6%, (min: 3.6%; max:17.7%) (38). Additionally, the noise-correlation matrix showed minimal noise-correlation between receive element 25 and the other receive elements. This shows that the noise-correlation measurements do not directly measure inter-element coupling if a receive element has lower sensitivity, such as element 25. Ideally, inter-element coupling would be measured by taking an S_{12} bench measurement between receive elements when they are connected to their isolation preamplifiers. However, in this situation this was not possible since the preamplifiers were located inside the Philips interface box. Overall, for the remaining 31 receive elements, individual element sensitivity patterns were similar, as shown in Figure II-12, and the noise-correlation matrix showed good isolation between receive elements, meaning that the combination of preamp decoupling and geometric decoupling was sufficient.
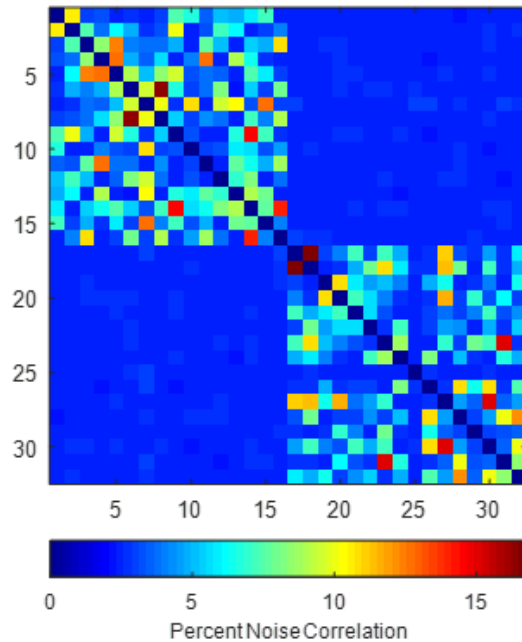
Figure II-13. Noise correlation matrix for 32- channel receive array with diagonal elements removed. The noise correlation matrix shows a mean noise correlation of 5.7% and maximum noise correlation of 16.5% for coils 1-16, and a mean noise correlation of 5.0% and a maximum noise correlation of 16.8% for coils 17-32.

II.4.5 g-factor Maps

G-factor maps were acquired for acceleration factors up to nine and demonstrated the feasibility of accelerated imaging without sacrificing excessive SNR (average g-factor < 1.2) for acceleration factors up to six (60). A middle axial slice of the SENSE g-factor maps for multiple acceleration combinations is shown in Figure II-14. Among these acceleration schemes, the average g-factor rose above 1.2 only when accelerating by factors of three in the foot/head direction. Even in these cases, the average g-factor reached a maximum of 1.23 for nine times acceleration. The shortest scan duration

within a mean g-factor of 1.2 was 45.1s, which is well within a clinically relevant 90s

scan duration.
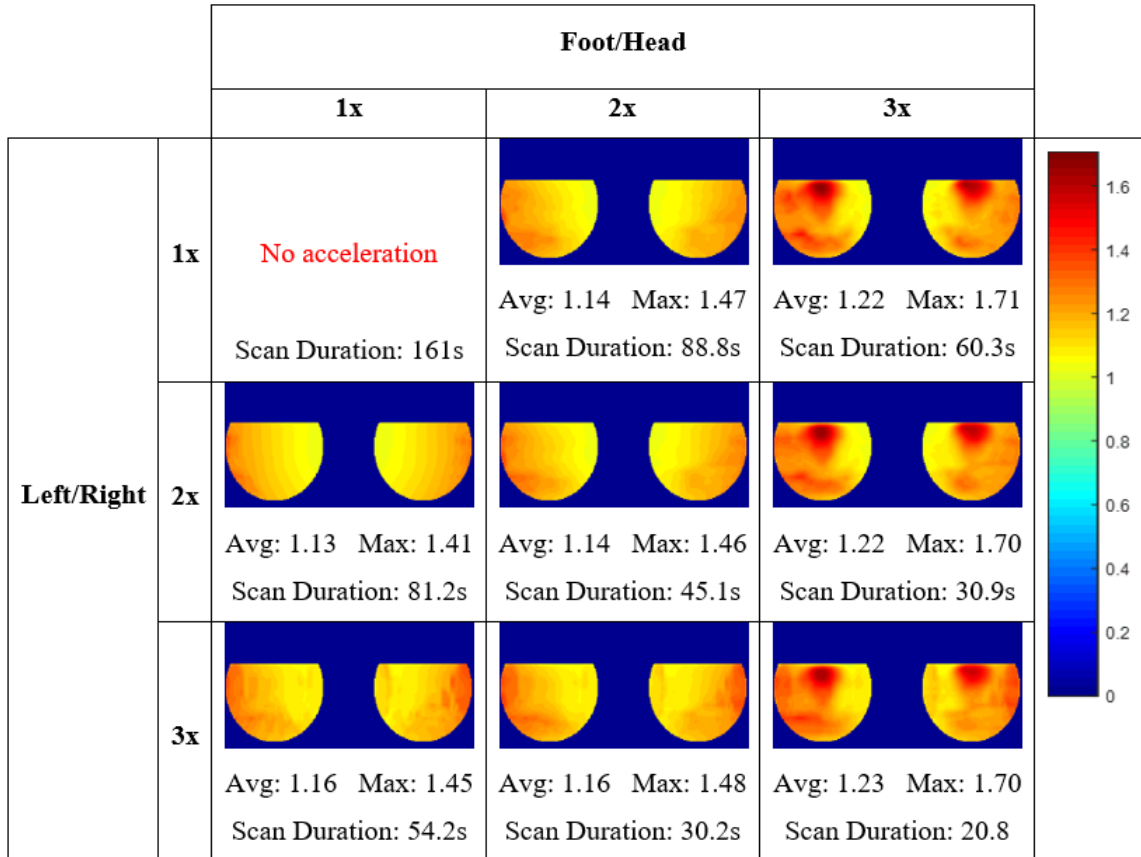
Figure II-14. g-factor maps for the 32-channel array for axial slices. Acceleration factors of 1x, 2x, and 3x in the foot-to-head direction and left-to-right direction were taken. Average and maximum g-factors are reported under each image, as well as the scan duration.

II.4.6 High Temporal and Spatial Resolution

High temporal resolution images (R=16; SD=10s; 1mm iso) and high spatial resolution images (R=4; SD=90s; 0.75mm iso) are shown for comparison to the volume coil in Figures II-15A-C. As detailed above, quantification of the image quality was calculated by taking a ratio of the mean signal in the zoomed region over the standard deviation of the same region after applying a high-pass filter. The image quality ratios of the high temporal resolution image (22.1), high spatial resolution image (31.1), and volume coil image (23.0) showed similar values, therefore indicating comparable image quality to the volume coil despite the increase in both temporal and spatial resolution. For reference, the non-accelerated array coil image is also shown in Figure II-15D with a measured ratio of 81.2.
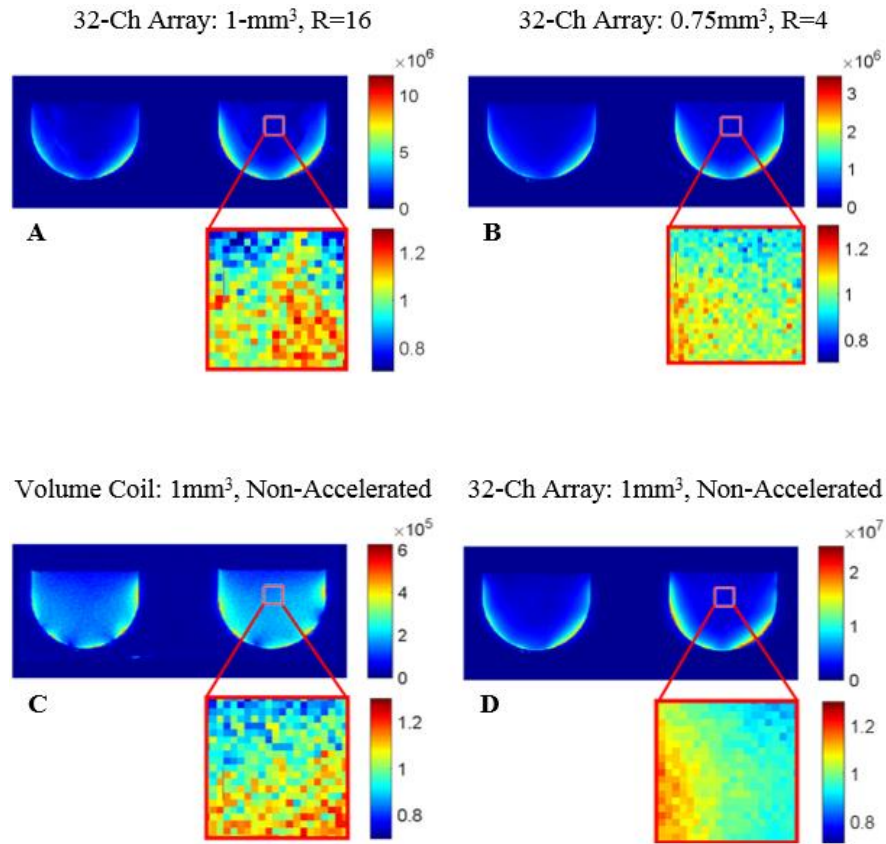
Figure II-15. Image quality comparison of non-accelerated and accelerated images. The high temporal resolution image (A) and accelerated high spatial resolution image (B) show comparable image quality to the volume coil image (C). The non-accelerated array coil image (D) is also shown for reference.

II.5 Conclusions

This work described the construction and evaluation of a bilateral 32-channel receive array and FCE volume coil for breast imaging at 7T. The use of the modified FCE design for integration of the receive array and active detuning network, detachable boards for each receive element, preamplifier decoupling network for high operating frequencies, and an addition of a passive-detuning trap simplified the construction and integration of receive and transmit elements. Evaluation of the FCE volume coil and 32-

channel coil array showed homogeneous excitation, significant improvements in SNR, and receive element isolation. Additionally, g-factor mapping showed the feasibility of accelerating up to a factor of six times while staying within acceptable g-factor values. Finally, an image with high resolution and an accelerated image with high spatial resolution showed the potential utility of the coil for acquiring images with high spatial and temporal resolutions for dynamic studies such as DCE-MRI and DWI.

CHAPTER III

CHARACTERIZATION OF DOUBLE-TUNED BIRDCAGE COILS FOR MR

IMAGING AND SPECTROSCOPY OF GOLDEN RETRIEVER MUSCULAR

DYSTROPHY TISSUE SAMPLES

III.1 Synopsis

Two double-tuned birdcage coils were constructed to further investigate the

potential value of magnetic resonance imaging and spectroscopy to study DMD in a

genetically homologous animal model, GRMD. Coil performance was evaluated on the

bench via S_{11} and S_{12} measurements, as well as on a 4.7T Varian Inova small animal

scanner. S_{11} measurements showed good matching and tuning, better than -20 dB for all

coil ports. S_{12} measurements showed good isolation (better than -17.7 dB) between all

coil ports and homogeneous field patterns (<10% variation in B_1^+) along the middle ~8

cm of the coil. Furthermore, ^{1}H images also showed signal homogeneity throughout the

center ~8 cm region-of-interest (mean: 1.06 ± 0.14), and X-nuclei imaging/spectroscopy

showed ability to distinguish between different biological concentrations of ^{23}Na and ^{31}P

in various phantoms.

III.2 Introduction

DMD is an X-linked recessive disorder affecting 1 in every 3500-5000 males

(61). This disorder causes progressive muscle degeneration due to lack of dystrophin

cytoskeletal protein, ultimately leading to death within the patient's late 20s or early 30s

(62,63). GRMD is a genetically-homologous animal model of DMD, which is why it is

of particular interest for treatment development and evaluation of DMD biomarkers (64-66). Large phenotypic variations in disease severity in both GRMD and DMD make noninvasive biomarkers particularly attractive since they enable studies of disease progression where each subject can be used as its own control (66,67). This has led to increased interest in the use of MRI and MRS to study GRMD with specific interest in ^{1}H MRI/S, ^{23}Na MRI, and ^{31}P MRS (19-30).

The goal of this study is to characterize two double-tuned birdcage coils used to further investigate the potential value of magnetic resonance imaging and spectroscopy to study DMD. Coil performance was evaluated via bench measurements and imaging/spectroscopy, for homogeneity and ability to distinguish between various phantoms with different [23]Na and ^{31}P concentrations. Overall, this chapter covers construction of custom hardware including two double-tuned birdcage coils and an associated positioning fixture, as well as coil characterization.

III.3 Methods

III.3.1 Hardware and Sample Holder Construction

Two double-tuned birdcage coils were designed based on the four-ring low-pass, high-pass configuration presented by Murphy-Boesch et al. (68). As shown in Figure III-1, the coil can be thought of as three separate structures, where the two outer structures are inductively coupled through the inner structure and resonate at the ^{1}H frequency, and the inner structure resonates at the Larmor frequency of the low-γ nucleus, either [23]Na or ^{31}P in this case. A low-pass, high-pass coil configuration, as well as the field patterns

52

produced by the coil are shown in Figure III-1, as reported by Murphy-Boesch et al. (68).
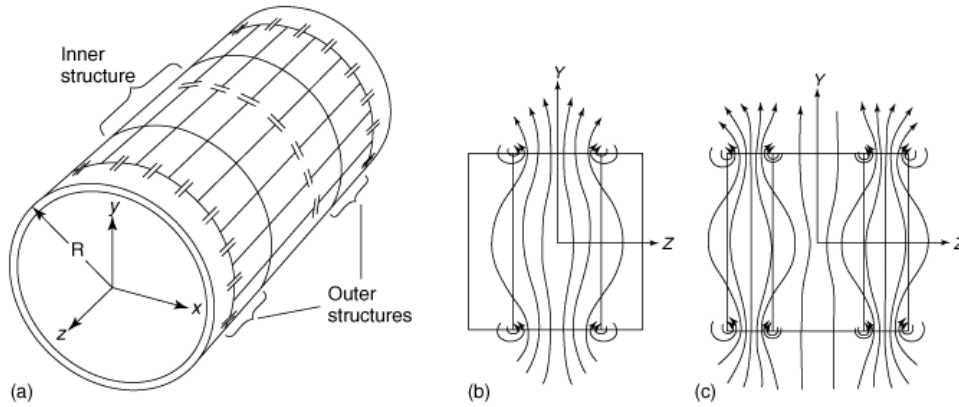
Figure III-1. Four-ring birdcage coil in a low-pass, high-pass configuration. A) The outer high-pass structures are resonant at the higher frequency, while the inner low-pass structure is resonant at the low-γ nucleus. B) The RF field patterns of the inner structure show a homogeneous region within the center of the coil with inhomogeneities close to the two inner endrings. C) The RF field patterns show that more field is produced within the two outer structures. However, due to inductive coupling of the outer structures, homogeneous ^1H fields are also produced at the center of the coil. Reprinted with permission of Elsevier from (68).

To minimize potential coil imbalances caused by asymmetry, each coil was milled on flexible copper-clad FR4 boards (board thickness: 0.18 mm) then carefully mounted on an acrylic tube (od: 7.6 cm); ensuring the boards were mounted straight and the edges of the board did not overlap. The length of the inner structure (12.5 cm) was larger than that of the 50 ml vial, which contained the muscle samples mentioned in

53

Chapter 4, to avoid placing any part of the sample coincident to the inner endrings, where inhomogeneities are present. The total coil length (25 cm) was then based on the inner structure length and the design presented in (68), where the total coil length consisted of 25% for each of the two outer structures and 50% for the inner structure, to avoid coupling of the low-pass and high-pass resonant modes. The coil outer diameter (7.6 cm) was selected to encompass the sample vial and reference phantoms needed for [23]Na imaging, and to place the sample away from the field inhomogeneities close to the coil rungs. The coil was shielded to minimize changes in the coil's resonant frequency when placed within the magnet bore. The RF shield was constructed of flexible copper-clad FR4 boards mounted inside an acrylic tube with an inner diameter approximately 1.5 times that of the birdcage coil (od: 11.9 cm). Finally, a sample holder was made to consistently position the sample at the axial center and concentric to the birdcage coil. Figure III-2 shows the RF shield, a double-tuned birdcage coil, and the sample holder with a vial in which the sample was placed in.
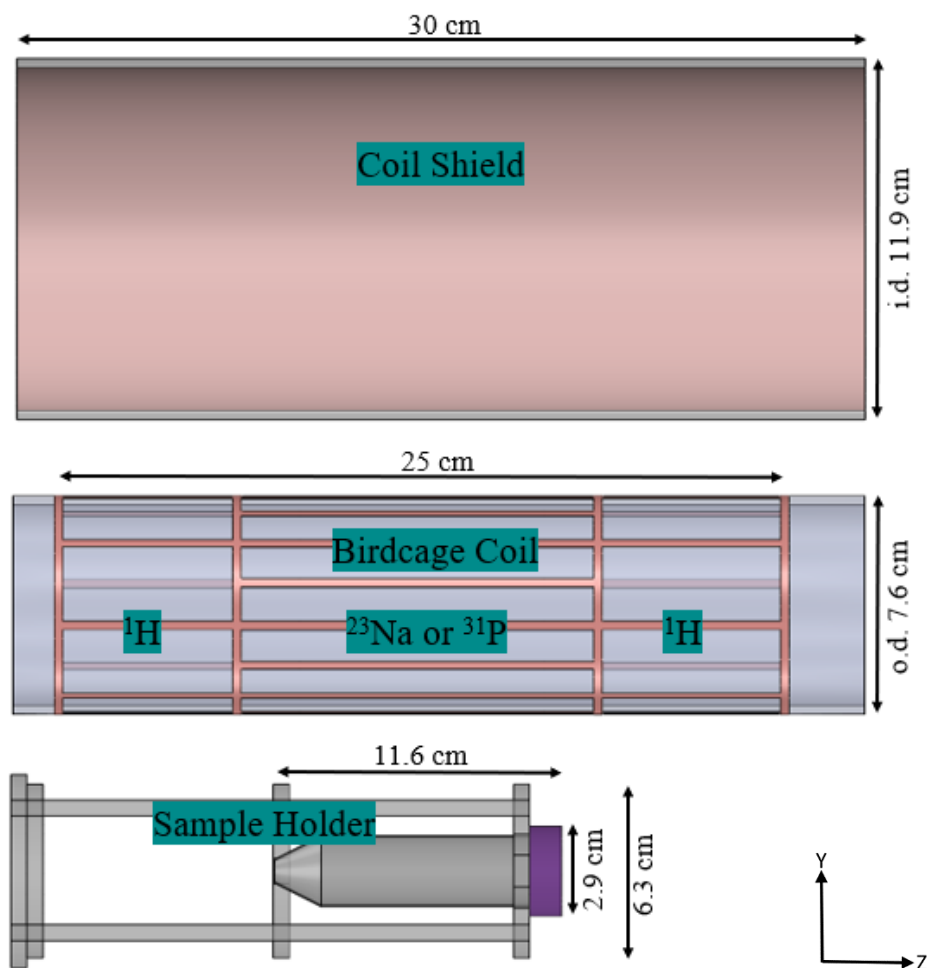
Figure III-2. Solidworks renderings of RF shield, birdcage coil, and sample holder.

Coil tuning capacitances were initially calculated using BirdcageBuilder software (69). The outer structures consisted of 8 legs and were tuned to 200 MHz (^{1}H at 4.7 T) in a high-pass configuration, while the inner structures consisted of 16 legs and were tuned to either 52.93 MHz (^{23}Na at 4.7 T) or 81 MHz (^{31}P at 4.7 T) in a low-pass configuration. Additionally, the "Leg Length" parameters entered in BirdcageBuilder for

the inner structures were 12.5 cm, and 7.5 cm for the outer structures. After inputting all

the remaining parameters such as: trace width, number of legs, coil configuration, etc.

capacitance values (C).needed to resonate both the inner and outer structures were

calculated.

The calculated capacitors needed to resonate at 52.93 MHz or 81 MHz were then

mounted on the inner structures of each coil while leaving the outer structures open

circuited. S_{12}, double-loop probe measurements were then taken to detect the resonant

frequency of the inner structures. Often the resonant frequency (f_{res}) based on the

calculated capacitance values was slightly off from the desired value, therefore Eq III.1-

Eq III.3 were used to calculate the capacitance values needed based on the measured

resonant frequency. To resonate the outer structures at 200 MHz, the capacitors from the

inner structures were replaced with copper tape (to represent a short) and the capacitors

of the outer structures placed on the two outer endrings. Similarly, if the coil was slightly

off resonance, Eq III.1- Eq III.3 were used to calculate the desired capacitance values.

$$\omega = B_0 \gamma \qquad \qquad \text{(Eq III.1)}$$

$$\omega = 2\pi f_{res} \qquad \qquad \text{(Eq III.2)}$$

$$\omega = 2\pi f_{res} = \frac{1}{\sqrt{LC}} \qquad \qquad \text{(Eq III.3)}$$

The capacitance values used to tune the outer structures to 200 MHz were

alternating 9.1/10 pF capacitors (1111C Series, Passive Plus), while the values used to

tune the inner structures to 52.93 MHz or 81MHz were 30 pF or alternating 12/13 pF (1111C Series, Passive Plus). Structures for the low-γ nuclei were driven in quadrature mode, to increase SNR, with variable capacitive matching networks (NMAT40HVE, Voltronics). Meanwhile, the ^{1}H structures were driven linearly because SNR was sufficient for ^{1}H imaging. Finally, double-tuned cable traps were placed on the co-axial lines to eliminate common-mode currents (70).

III.3.2 Tissue Phantoms

Tissue phantoms were made to mimic biological concentrations of ^{23}Na and ^{31}P within skeletal muscle (25,71). To characterize the ^{1}H/^{23}Na coil, five ^{23}Na phantoms contained within 50 ml vials, with concentrations ranging from 0 mM to 80 mM (increments of 20mM) were made of NaCl aqueous solution. Additionally, two reference phantoms contained within 3D printed shells were constructed to use as signal references throughout ^{23}Na and ^{1}H imaging experiments. These reference phantoms both had a sodium concentration of 50 mM, with one phantom made of NaCl aqueous solution and the other gelatinized with 5% agarose to mimic the sodium ion mobility within the extracellular and intracellular compartments, respectively (25,72).

Two ^{31}P phantoms with phosphorus concentrations of 20 mM and 40 mM were used to characterize the ^{1}H/^{31}P coil. These phantoms were composed of phosphoric acid solution (345245-100ML, Sigma Aldrich); therefore, were a source of inorganic phosphate (Pi). Similarly, a 3D printed, reference phantom with a Pi concentration of 40 mM was constructed.

III.3.3 Bench Measurements

Bench measurements were performed on a network analyzer (Agilent, E5017C) to assess the performance of both birdcage coils. S_{11} measurements were taken to analyze the matching and tuning at all ports, as well as the quality factor of the coils under unloaded and loaded conditions. Specifically, loaded S_{11} measurements on the $^1H/^{23}Na$ coil were taken with one of the tissue samples (L: S) and with the tissue sample and both sodium reference phantoms (L: S+P). The $^1H/^{31}P$ coil loaded measurements were take with the same tissue sample (L:S) and the tissue sample and 40 mM phosphorus phantom (L: S+P). The quality factor (Q) of the coils was then calculated (based on the S_{11} measurements of all ports) in standard fashion, as shown in Eq III.4. As described by Doty et al. (73), Δf_{7dB} is the bandwidth at which the reflection coefficient of the coil (S_{11}) is 7 dB below the baseline, while f_{res} is the resonant frequency of the coil. Ultimately, Q-factors are used to measure the efficiency of a coil to detect MR signals.

$$Q = \frac{f_{res}}{\Delta f_{7dB}} \qquad\qquad (Eq\ III.4)$$

S_{12} measurements were used to analyze the isolation between ports. Additionally, field measurements were taken while transmitting through the coil and detecting the transmitted signal through a pickup probe along the coil's length to assess the coil homogeneity along the axial direction. Lastly, S_{12} measurements, using current-injection

probes, were taken to measure the common-mode attenuation of the double-tuned baluns.

III.3.4 Imaging and Spectroscopy

Images and spectra were acquired using a 4.7T Varian Inova scanner. As a signal reference, the two sodium reference phantoms were placed around the 50 ml vial when imaging both ^{1}H and ^{23}Na. For evaluation of ^{1}H performance when using the ^{1}H/^{23}Na coil, sixteen 1 mm transverse slices (with a slice gap of 9 mm) were acquired to test the transverse and axial coil homogeneity throughout the entire phantom. Due to long imaging times when imaging ^{23}Na, a coronal slice was acquired to assess the homogeneity of the X-nuclei in the ^{1}H/^{23}Na, in place of multiple transverse slices.

^{23}Na images and ^{31}P spectra were acquired on all the phantoms previously mentioned to test the coils' ability to distinguish between different sodium or phosphorus concentrations. The parameters used to acquire images and spectra are listed in Table III-1.

	¹H	²³Na	³¹P
Sequence	SEMS	GEMS	SPULS
TR (ms)	750	100	1000
TE (ms)	16	3.9	-
FOV (mm)	96x96	192x192	-
Slice Thickness (mm)	1	6	-
Matrix Size	128x128	64x64	-
Number of Averages	1	150	100
Scan Duration (m:s)	1:36	16:02	1:39

Table III-1. Imaging parameters used to characterize coils (SEMS: spin echo multi-slice; GEMS: gradient echo multi-slice; SPULS: 1-D pulse and acquire sequence)

III.3.5 Image and Spectra Processing

Images and spectra were processed using custom Matlab scripts. A region growing algorithm was used on ¹H images to segment the distilled water phantom (within the 50 ml vial) located at the center of all transverse slices. ¹H homogeneity was assessed based on the average of the segmented region throughout all slices, except for the slices outside of the phantom region.

Both coils were evaluated for their ability to distinguish between various phantoms with different sodium and phosphorus concentrations. As previously described, during ²³Na imaging, the two sodium reference phantoms were consistently placed surrounding the 50 ml vials throughout all images. Meanwhile, the 50 ml vials with different sodium concentrations were exchanged before each image. Sodium concentrations, within the 50 ml vials, were measured based on their relative signal

(average signal within ROI of 50 ml vial / average signal within ROI of aqueous solution

sodium reference phantom). Before analysis, all ^{31}P spectra were manually zeroth-order

phase-corrected. Relative SNR (integral under the curve / standard deviation of the

noise) was used to calculate the Pi concentrations of both phantoms.

III.4 Results and Discussion

III.4.1 Hardware and Sample Holder Construction

An isometric view of one of the two birdcage coils is shown inside the RF shield

in Figure III-3 (left). The same RF shield was used for both birdcage coils and had an

acrylic lid on the distal end (not shown in Figure) with a locking mechanism to ensure

the coils were consistently placed within the same region. The front end of the coil

shows the tuning rods, which are connected to the tuning and matching capacitors of

each port to allow tuning and matching of the coil once placed within the shield. An

additional acrylic piece was added to provide mechanical stability to the double-tuned

baluns. The phantom setup is shown in Figure III-3 (right), with the 50 ml vial at the

center of the phantom holder and the two 3D printed reference phantoms concentrically

oriented.
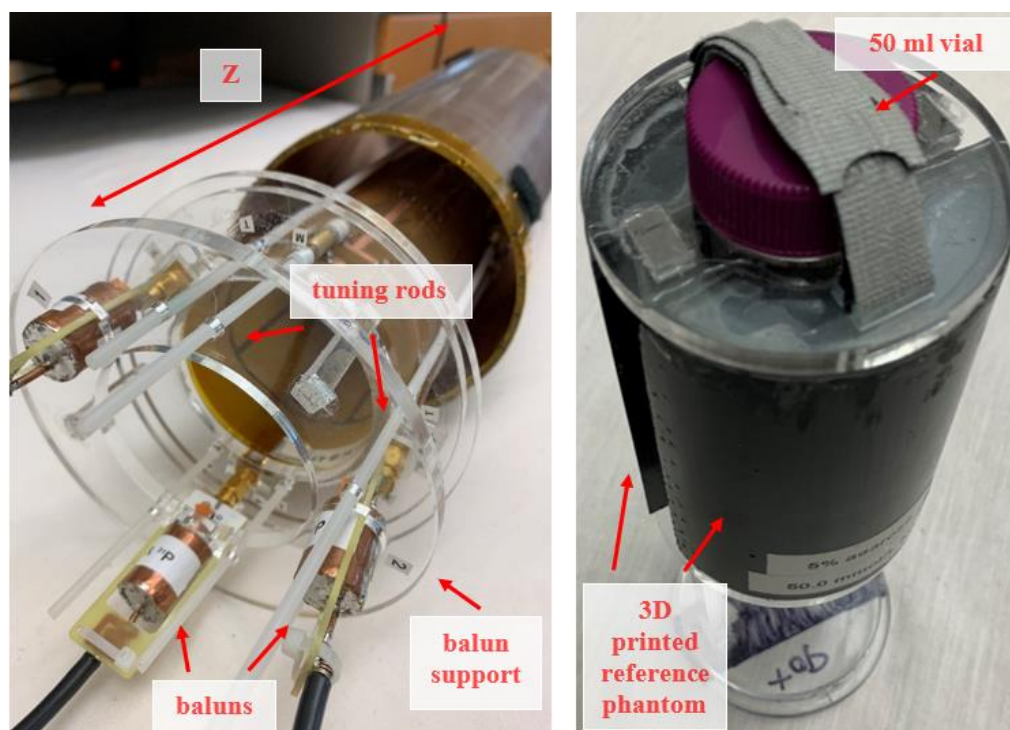
Figure III-3. Birdcage coil and phantom setup. For visibility, the birdcage coil was slightly pulled outside of the RF shield (left). The full coil setup includes: tuning rods, baluns with coaxial cables, and an acrylic balun support. The phantom set up (right) shows the sample positioner with a 50 ml vial located at the center and two 3D printed reference phantoms concentrically oriented. A Velcro strap (shown in gray) was used to keep the 50 ml vial in place.

III.4.2 Bench Measurements

Bench measurements showed good matching and tuning of both coils at all ports, with S_{11} measurements better than -20.6 dB in all cases. Additionally, the coil could be tuned and matched, even when loaded, by simply modifying the capacitance of the variable capacitors. S_{11} measurements at both frequencies of the ^1H / ^{23}Na coil, and of the ^1H / ^{31}P coil are shown in Figure III-4. Overall, good coil behavior was observed when matching and tuning the coils, with little to no coupling between the three ports.

This can also be explained by the isolation measurements for all ports, with S_{12} measurements better than -17.7 dB in all cases.
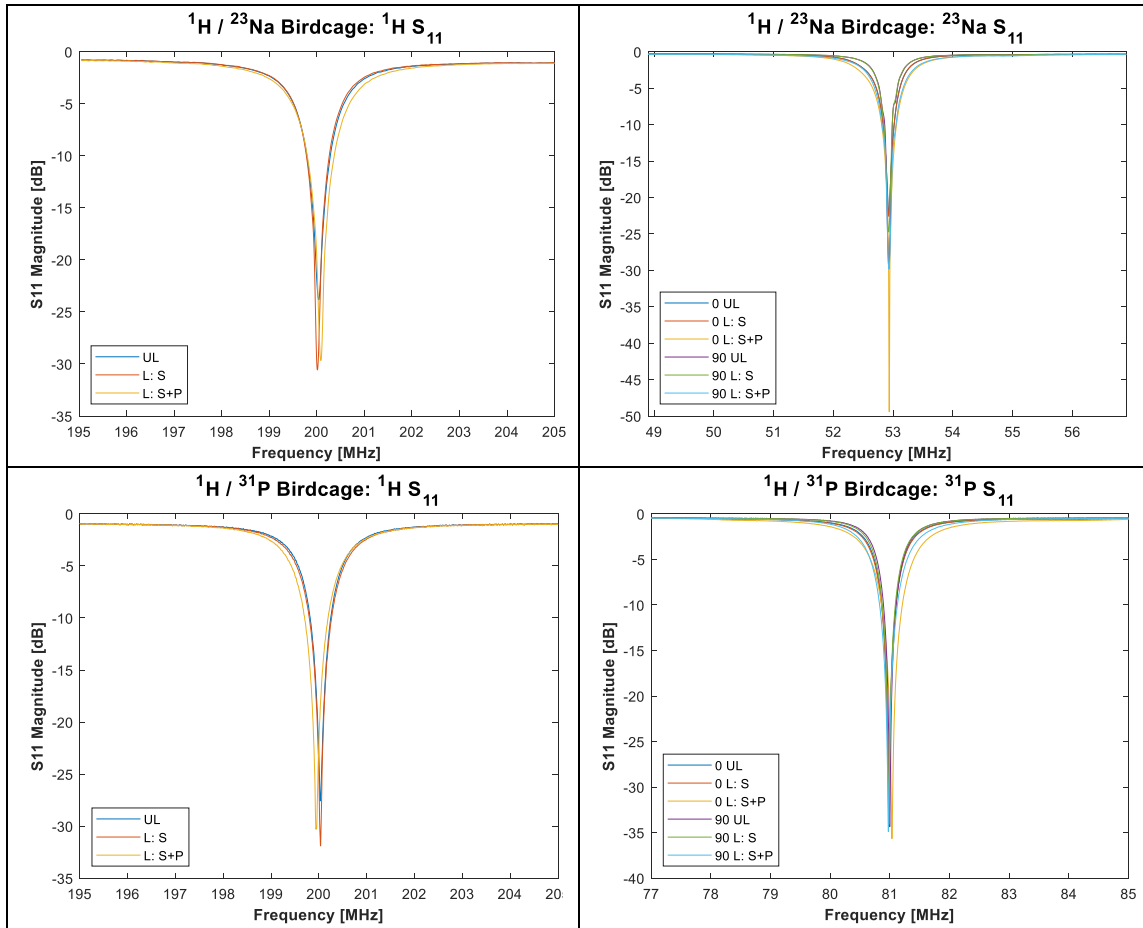
Figure III-4. S_{11} measurements at all ports of both birdcage coils. S_{11} measurements were acquired in both unloaded and loaded states. The loaded states were either loaded just with a rectus femoris tissue sample (L: S) or with the same tissue sample and the reference phantoms (L: S + P). Good matching and tuning was shown in all cases.

Q measurements, as described in Eq III.4, were then calculated based on the S_{11} measurements. All Q measurements are reported in Table III-2 for both unloaded and loaded states. As shown, Q did not change much (and even increased in some cases) when the coil was loaded with just the tissue sample. However, there was an observable decrease in Q as the loading increased, or when the reference phantoms were added. This shows that the coil-noise dominated the tissue sample-noise, therefore resulting in a decrease in SNR (34). This can likely be attributed to the size of the coil relative to the tissue sample.

		Q Measurements		
		0° Port	90° Port	^{1}H Port
^{1}H / ^{23}Na Coil	Unloaded	187	234	266
	Loaded: S	187	248	274
	Loaded: S + P	141	156	233
^{1}H / ^{31}P Coil	Unloaded	227	253	303
	Loaded: S	220	248	281
	Loaded: S + P	154	181	269

Table III-2. Unloaded and loaded Q measurements of both coils. Q measurements were taken based on the S_{11} plots shown in Figure 4. High Q values were observed in all cases. However, Q ratios ($Q_{loaded}/Q_{unloaded}$) were not greater than two in any case.

S_{12} measurements of all double-tuned baluns were acquired using a current-injection probe. As shown in Figure III-5, the common-mode attenuation for all double-tuned baluns was at least -20.8 dB, with values pertaining to the ^{1}H frequency better than those for the X-nuclei in both cases. Overall, all three double-tuned baluns yielded consistent values at both frequencies.
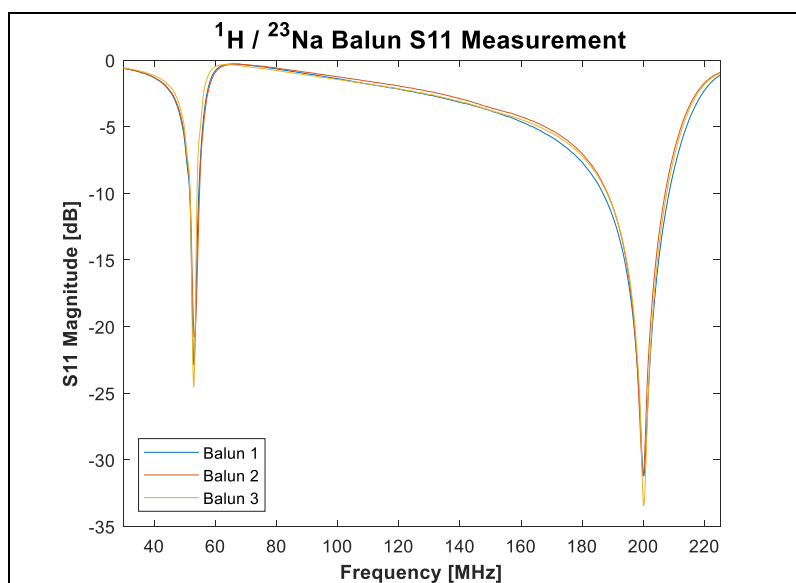
Figure III-5. S_{12} measurements of double-tuned baluns. S_{12} measurements of all six double-tuned baluns showed good common-mode attenuation, with values ranging from -20.8 dB to -37.1 dB.
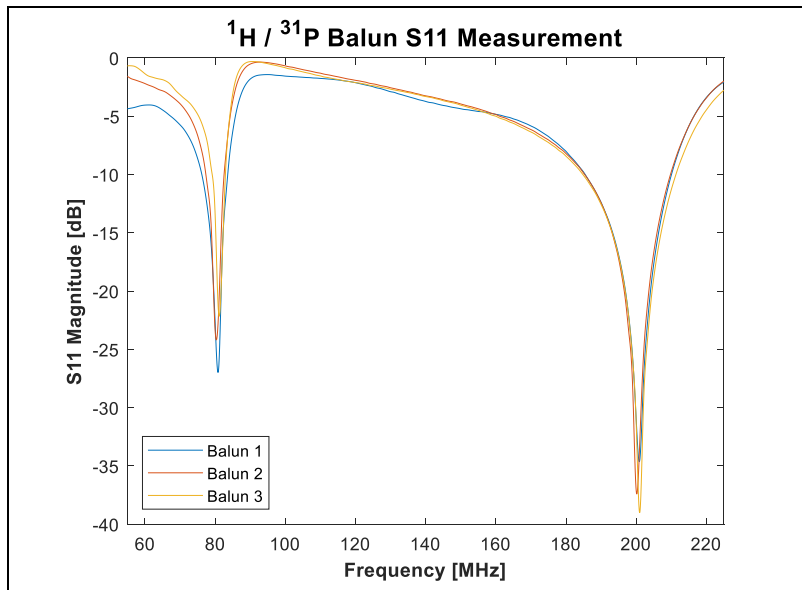
Figure III-5 Continued.

Field measurements along the long-axis showed <10% variation in B_1^+ field for both nuclei in both coils along the middle ~8 cm, as shown in Figure III-6. Outside of that region large variations in the B_1^+ field were measured due to endring currents from the low-γ nuclei structures, as expected (68). S_{21} measurements showed a correlation with the patterns previously mentioned and shown in Figure III-1. Specifically, the inner structures of both coils, pertaining to the X-nuclei, drop off significantly as they approach the endrings, while the two outer structures, pertaining to ^{1}H, produce more field within their structures and less towards the middle portion of the coil. Overall, homogeneity was observed throughout an ~8 cm the region of interest, with inhomogeneities present close to the inner endrings.
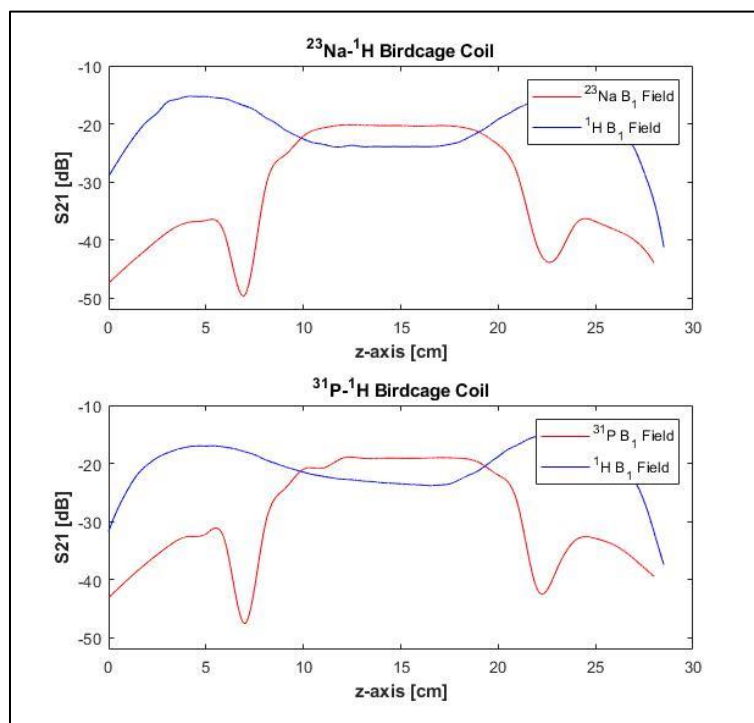
Figure III-6. B_1^+ field along long-axis of birdcage coils. The (top) plot shows the B_1^+ field pertaining to both frequencies of the ^1H / ^{23}Na birdcage coil, while the (bottom) shows the B_1^+ field pertaining to both frequencies of the ^1H / ^{31}P birdcage coil

III.4.3 ^1H Imaging

Sixteen ^1H transverse slices were acquired to assess coil homogeneity throughout the entire distilled water phantom located at the center of the coil, in a 50 ml vial, as shown in Figure III-7. Mean signal values were calculated after segmenting the signal pertaining to the middle phantom. These values showed an overall mean of 1.12 ± 0.44, or a variation in the mean value of about 40%. Since large variations were mostly present at the outer edges, this was also calculated over the center 8 slices (Slices 5-12).

67

This showed an overall mean of 1.06 ± 0.14, or a variation of 13%, closely matching the

bench measurements shown in Figure III-6.
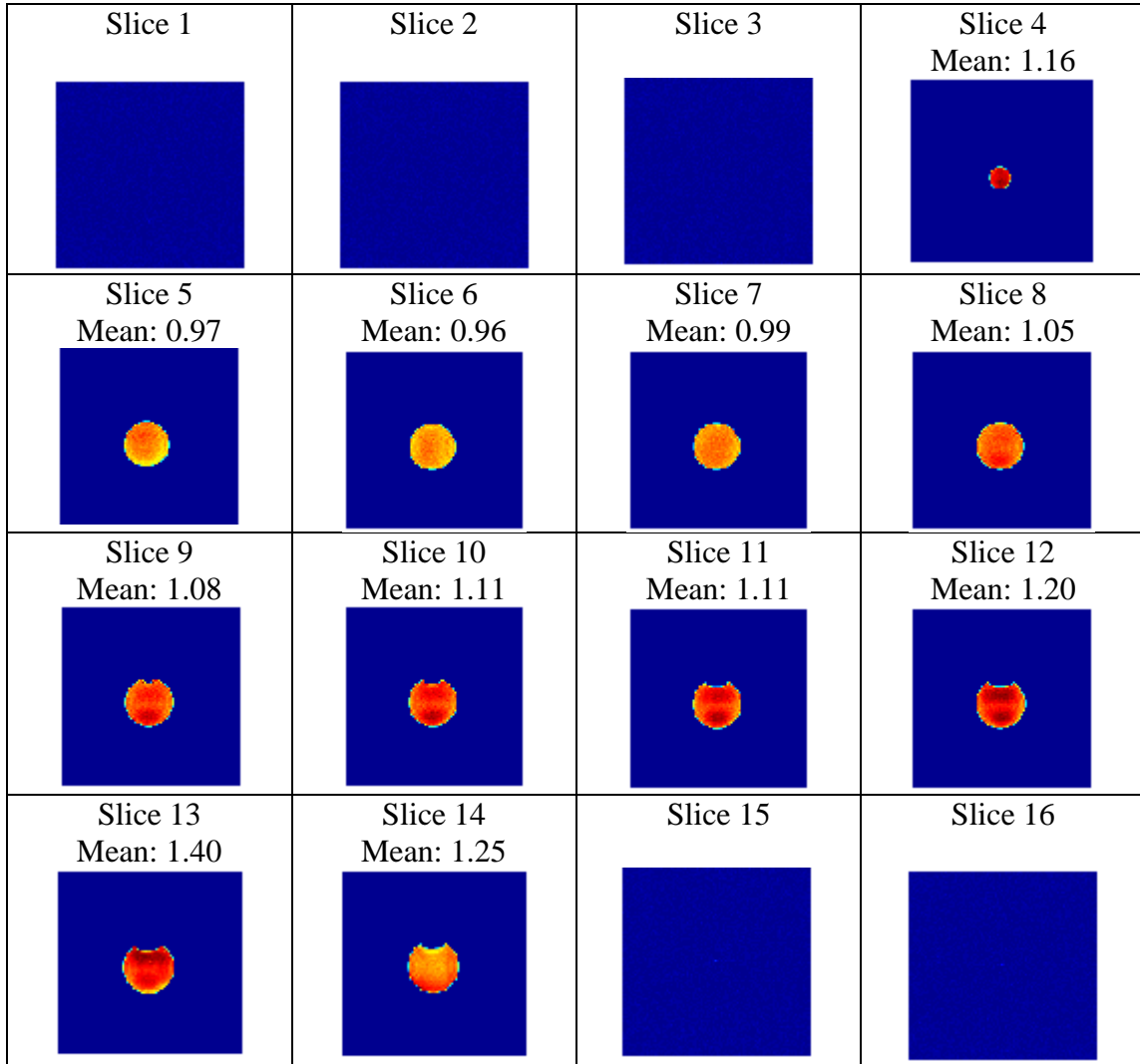
Figure III-7. Sixteen ^{1}H transverse slices. Each 1mm slice was acquired with a slice gap of 9 cm, meaning the overall distance covered was 16 cm, with the first three and the last two slices and the last out of the range of the phantom. Slice 4 is located at the apex of the conical part of the vial, while Slice 14 is at the vial lid (refer to Figure III-2 for location reference).

III.4.4 ^{23}Na Imaging

Due to long imaging times of ^{23}Na images, ^{23}Na signal homogeneity of the inner structure was assessed on a coronal image and a profile through the center of that image, as shown in Figure III-8. The ^{23}Na coronal image shows the 80 mM sodium phantom in a 50 ml vial (center), the aqueous solution sodium reference phantom (left), and the gelatinized sodium reference phantom (right). Despite the inherently low SNR of ^{23}Na images, the coronal image appears homogenous throughout most of the center phantom with inhomogeneities mostly present at the edges, or towards the endrings, as expected (68,72). The mean signal throughout the middle 8 cm of the phantom was 77.8 (min: 53.7, max: 100). The profile taken through the center of the 80 mM phantom (location marked by black dashed line on image), showed a minimum signal value of 70 and maximum of 98 throughout the middle 8 cm of the profile, meaning there was no more than 29% variation throughout the profile.
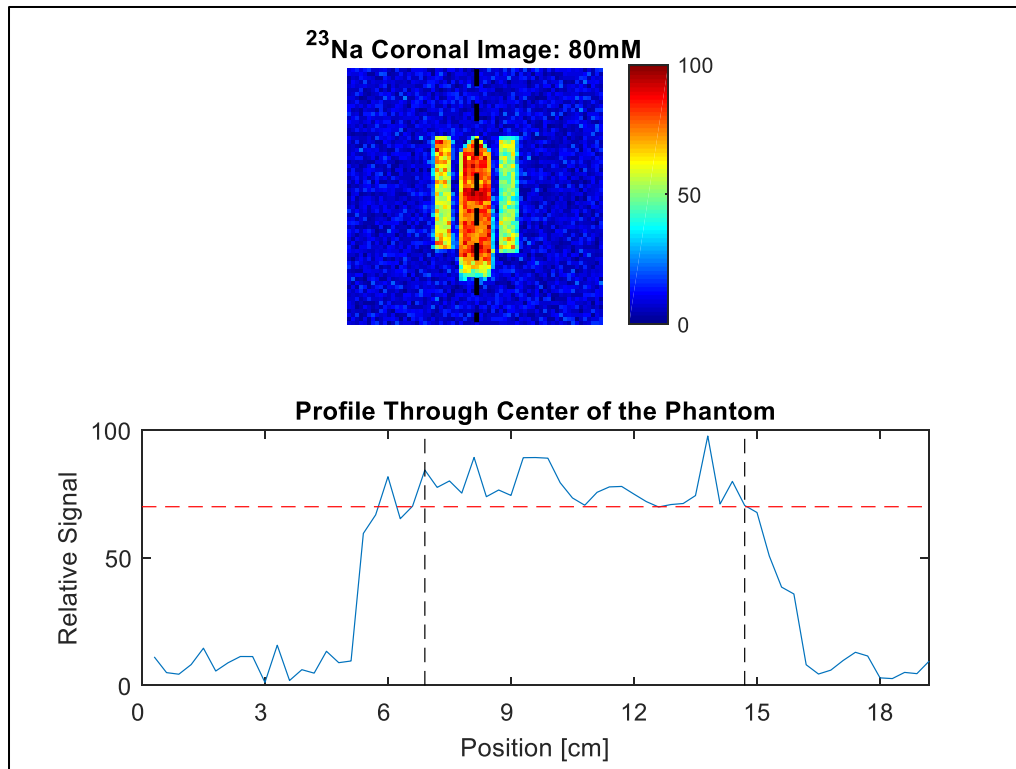
Figure III-8. ^{23}Na imaging for assessment of coil homogeneity. The coronal image appears homogenous throughout the middle region, with inhomogeneities mostly present at the outer edges of the long axis. A profile was taken along the center of the coronal image (location marked by dashed black line on image). The minimum (red dashed line on profile) and maximum signal were then evaluated within the middle 8 cm of the profile (black dashed lines on profile).

The coil was then assessed for its ability to distinguish between various phantoms with different sodium concentrations. Five sodium transverse images are shown on Figure III-9, with sodium concentrations of the center phantom ranging from 0 mM to 80 mM. The ^{23}Na relative signals were then calculated for each image by taking the ratio of the average signal of the center phantoms over the average signal of the

70

aqueous solution reference phantom (reference phantom on the right). A plot displaying

the relative signal versus the known sodium concentration of the sodium phantoms

shows a linear correlation ($R^2 = 0.97$). Therefore, this demonstrates the coils ability to

determine relative sodium concentrations.
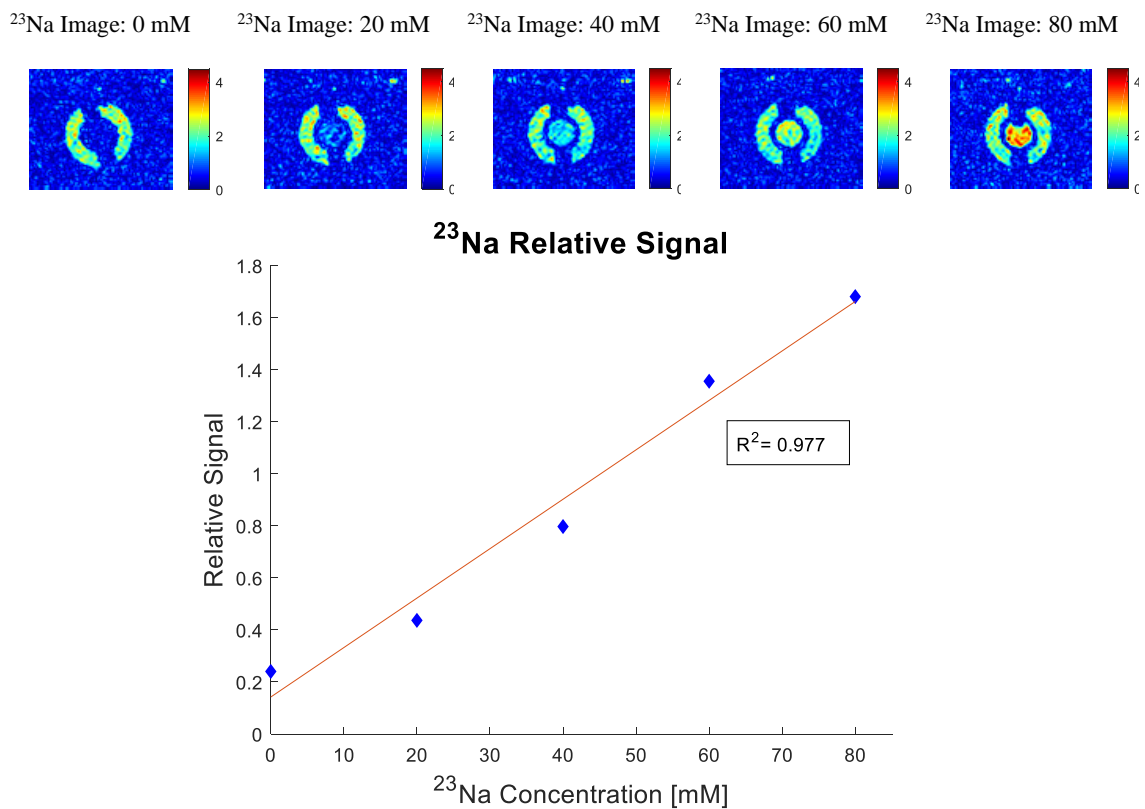
Figure III-9. ^{23}Na imaging of phantoms with various sodium concentrations. The five ^{23}Na transverse images are all displayed on the same scale. Observable increases in signal within the center phantoms are shown throughout the images, as sodium concentrations increase. Furthermore, the plot shows that the relative signal increases linearly with the phantom sodium concentration.

III.4.5 ^{31}P Spectroscopy

The ^{1}H/^{31}P coil was mostly used for ^{31}P spectroscopy, with ^{1}H solely used for

scout images (to ensure proper coil and phantom placement) and shimming. Therefore,

coil performance was evaluated based on phosphorus spectroscopy. Before evaluating

phantoms with different concentrations, ^{31}P spectra were acquired with different number

of averages (N_{avg}), as shown in Figure III-10A. A decrease in noise (relative to the

maximum peak height) was observed as the number of averages increased, as expected.

Due to the high SNR observed at 100 averages, this parameter was used to acquire

spectra for both phantoms with different concentrations. An increase in peak height was

observed in the 40 mM ^{31}P phantom, in comparison to the 20 mM ^{31}P phantom, as

shown in Figure III-10B.
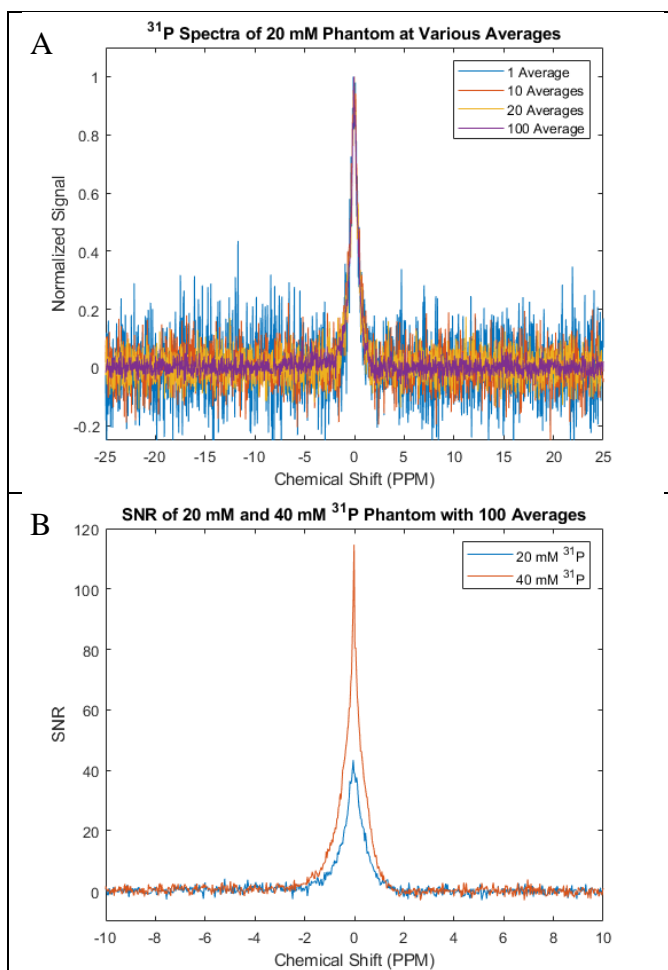
Figure III-10. ^{31}P spectra over different number of averages and concentrations. A) ^{31}P spectra was acquired on a phantom with a Pi concentration of 20 mM with different number of averages. Averaged spectra were normalized to their respective maximum signal value to show the noise relative to the maximum signal. B) Based on the high SNR observed at 100 averages, this was then used to acquire spectra of both phantoms with different concentrations. Each spectra was then divided by the standard deviation of their noise, therefore displaying SNR on the vertical axis.

Relative SNR measurements for all spectra are shown in Table III-3 below. These measurements were normalized by setting the highest SNR from each dataset to 1, in order to show the SNR values relative to each other. As shown by the relative SNR

73

values when averaging, the SNR increased with the number of averages; however, they

did not increase as expected, with the $\sqrt{N_{avg}}$ (34). This is perhaps due to the repetition

time used (TR = 1000 ms), meaning that the spins may have not fully relaxed back to

equilibrium between acquisitions. The relative SNR measurements at different Pi

concentrations of 20 mM and 40 mM were 0.52 and 1, respectively. These relative SNR

values closely matched to the expected value of 2, since the concentration doubled while

the volume of the phantom stayed the same. This showed the coil's ability to distinguish

between both phantoms of different concentrations.

	Pi Concentration	Number of Averages	Relative SNR
Relative SNR when averaging	20 mM	1	0.19
		10	0.40
		20	0.50
		100	1
Relative SNR w/ different concentrations	20 mM	100	0.52
	40 mM	100	1

Table III-3. SNR measurements of ^{31}P spectra. SNR measurements of spectra with different averages did not show the expected increase in SNR. However, when comparing the spectra pertaining to different Pi concentrations, the relative SNR values closely matched what was expected.

III.5 Conclusions

Ultimately, custom RF coils were constructed to acquire ^{1}H images, ^{23}Na images, and ^{31}P spectra to assess rectus femoris muscles from GRMD models. Coil performance was evaluated via bench measurements and imaging/spectroscopy on various tissue phantoms. Overall good coil performance was shown, with coil homogeneity observed along the center ~8 cm of both coils in all bench measurements and ^{1}H/^{23}Na images. Additionally, X-nuclei imaging and spectroscopy showed the coils' ability to distinguish between different biological concentrations of ^{23}Na and ^{31}P in various phantoms. While this chapter focused on characterization of the coils, Chapter 4 focuses on MRI and MRS of the rectus femoris muscle samples as well as correlations of NMR indices with age.

CHAPTER IV

BIOMARKER CHARACTERIZATION IN GOLDEN RETRIEVER MUSCULAR

DYSTROPHY TISSUE SAMPLES[2]

IV.1 Synopsis

Seven rectus femoris muscle samples (AUP: 2018-0182) from dogs with ages ranging from 3 to 30 months were studied. [1]H T1-weighted (T1w) and T2-weighted (T2w) images, [23]Na images, and ^{31}P spectra were acquired for each sample. [1]H T1w and T2w images showed a decrease in T2w/T1w signal ratio for the four older ($\geq$12 months) samples when compared to younger samples. Other NMR indices unexpectedly showed no significant correlation with age. The fixation process of the samples and varying levels of disease severity may have attributed to these results. Regardless, the associated custom coils and positioner developed to enable multi-nuclear studies will enable future work to investigate NMR-based biomarkers in the numerous GRMD samples available to our group.

IV.2 Introduction

Previous studies have shown variations in disease severity in genetically-homologous animal models of DMD, or GRMD (66,67). Therefore, noninvasive biomarkers are particularly attractive for studying disease where each subject could be used as its own control. This has led to increased interest in the use of MRI and MRS to

---

study GRMD with specific interest in ^{1}H MRI/MRS, ^{23}Na MRI, and ^{31}P MRS to monitor disease progression and treatment efficacy (19-30).

[1]H imaging and spectroscopy are useful techniques for assessing disease progression in DMD patients due to their ability to detect fatty infiltration and edema in rapidly progressing skeletal muscles (21-24). Specific ^{1}H biomarkers most commonly used are: muscle fat fraction (from ^{1}H spectroscopy of water and fat) and T_2 signal elevation (from [1]H T2-weighted images). However, due to the short lifespan of GRMD models, fatty infiltration is a less useful biomarker since death usually occurs before notable fatty infiltration (64-66,74,75). Instead, other ^{1}H biomarkers such as: elevated T_2 levels, increased T_2 heterogeneity, and increased T2-weighted/T1-weighted (T2w/T1w) signal ratios have all been used to assess GRMD (64-66).

In studies utilizing [23]Na MR imaging to assess DMD, consistent increased muscular total sodium concentration (TSC) and intracellular sodium concentration have been observed in subjects throughout all ages, even before fatty infiltration (25-27). This makes [23]Na imaging a potentially valuable tool for assessing disease progression throughout all stages of the disease. [31]P MR spectroscopy has also been used to study skeletal muscle of DMD and GRMD, with various differences including: increased inorganic phosphate (Pi) and phosphodiesters (PDE), and decreased phosphocreatine (PCr) observed between diseased patients and controls, as well as between non-ambulant and ambulant patients (20,28,29).

For [23]Na imaging, ^{1}H imaging capabilities are important to eliminate sample repositioning to ensure spatial correlation of both ^{1}H and [23]Na biomarkers. Additionally,

for spectroscopy studies, ^{1}H capabilities are important for shimming and acquiring scout images. This means double-tuned coils are particularly attractive for both ^{23}Na and ^{31}P studies. The goal of this study was to evaluate potential biomarkers in ten excised, formalin-fixed GRMD rectus femoris muscles.

IV.3 Methods

IV.3.1 Rectus Femoris Tissue Samples

Initially, images and spectra of ten rectus femoris tissue samples, shown in Table IV-1, were acquired and analyzed. However, due to significant differences in signal achieved from the three tissue samples underlined in Table IV-1, only the remaining seven tissue samples were used to study the effects of age on selected NMR indices. As shown in Table IV-1, the affected three samples were all excised and formalin fixed within a couple of weeks from each other, unlike the remaining seven samples.

Sample #	GRMD Name	Age	Gender	Date of tissue extraction	Volume (cm³)
_1_	**_Janet_**	**_1 yr_**	**_F_**	**_02/06/18_**	**_28_**
2	Red	6 mo	F	05/01/17	18
_3_	**_Sheldon_**	**_6 mo_**	**_M_**	**_02/13/18_**	**_20_**
_4_	**_Dory_**	**_6 mo_**	**_F_**	**_02/05/18_**	**_25_**
5	Chimy	2 yr	M	11/07/16	37
6	Revolver	6 mo	F	07/26/16	12
7	Cristal	2.5 yr	F	12/06/17	25
8	Patti	1 yr	F	02/04/14	30
9	Otis	1 yr	M	02/04/14	39
10	Frank	3 mo	M	02/15/07	23

Table IV-1. Rectus femoris muscle tissue samples from GRMD models. Images and spectra from tissue samples which are underlined (sample 1, sample 3, and sample 4) were not used to analyze the effects of age on selected NMR indices.

IV.3.2 Imaging and Spectroscopy

[1]H images, [23]Na images, and ^{31}P spectra were acquired using a 4.7T Varian Inova scanner and custom hardware including two double-tuned birdcage coils and an associated positioning fixture, as discussed in Chapter 3. As a signal reference, two phantoms containing 50mM NaCl (one aqueous solution and one gelatinized with 5% agarose to mimic sodium ion mobility within muscle) were placed around the tissue vial when imaging, as shown in Figure IV-1 (25). Additionally, to confirm the single peak observed in ^{31}P spectra of the tissue samples pertained to phosphocreatine (PCr), a 40 mM ^{31}P reference phantom was used when acquiring ^{31}P spectra for the first tissue sample (76).
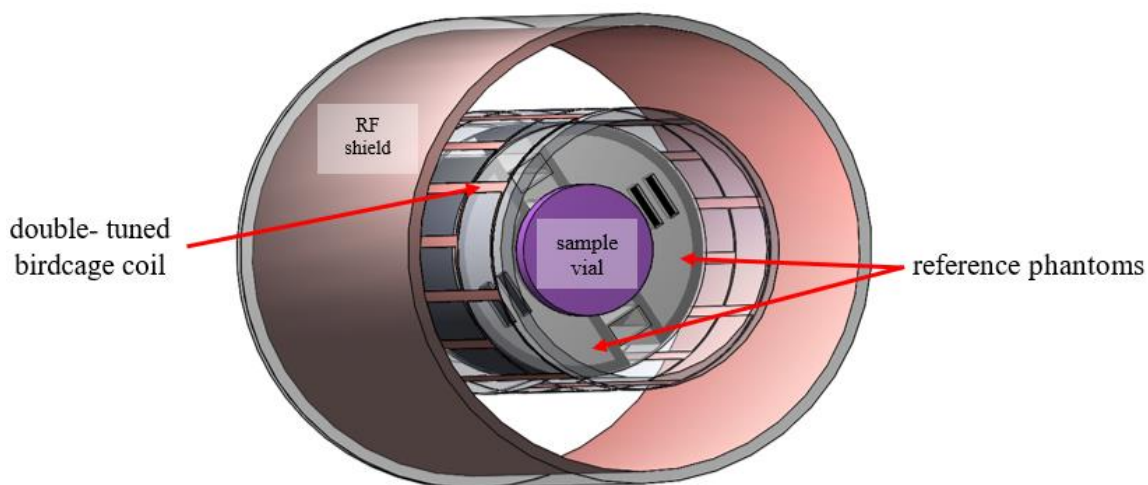
Figure IV-1. Solidworks rendering of complete imaging setup. The RF shield is mounted inside the outermost acrylic former and extends throughout the entire length of the coil. Meanwhile the coil, sample holder, reference phantoms, and sample vial are all concentric to the shield and in close proximity to each other.

T_1 and T_2 were calculated for ^1H and ^{23}Na in a single sample after incrementally varying TE or TR, respectively. Based on T_1 and T_2 values, appropriate imaging parameters were chosen for the remaining samples. For T1-weighted ^1H images, the shortest possible echo time (TE) of 16 ms and a repetition time (TR) of 750 ms (based on tissue T_1) were used. Meanwhile, for T2-weighted ^1H images, a longer TE (based on tissue T_2) and a long TR (approximately five times tissue T_1) was used. These imaging parameters allowed for T_1 and T_2 image weighting, while minimizing unwanted effects caused by either B_0 inhomogeneities or partial signal saturation, respectively (31). For ^{23}Na imaging, T_1 was also calculated in order to minimize partial signal saturation caused by a short TR, while staying within a reasonable imaging time. This is especially

80

significant in ^{23}Na imaging, since multiple averages are necessary in order to acquire images with sufficient SNR.

^{1}H reference images with the same resolution as the ^{23}Na images were also acquired to assist in segmentation of the tissue, phantom, and noise regions in the ^{23}Na images. Additionally, ^{31}P spectra were acquired using a pulse-and-acquire sequence (TR – 1000 ms; spectral resolution – 10 Hz; NSA – 500; scan duration – 8 min, 19 sec). The imaging parameters used to acquire images and spectra of the rectus femoris muscles are shown in Table IV-2.

	^{1}H T1w	^{1}H T2w	^{23}Na	^{31}P
Sequence	SEMS	SEMS	GEMS	SPULS
TR (ms)	750	4250	100	1000
TE (ms)	16	45	3.9	-
FOV (mm)	96x96	96x96	192x192	-
Slice Thickness (mm)	1	1	6	-
Matrix Size	128x128	128x128	64x64	-
Number of Averages	1	1	150	500
Scan Duration (m:s)	1:36	9:04	16:02	8:19

Table IV-2. Imaging parameters used to image rectus femoris samples (SEMS: spin echo multi-slice; GEMS: gradient echo multi-slice; SPULS: 1-D pulse and acquire sequence)

IV.3.3 Image and Spectra Processing

Images were segmented into separate tissue sample and phantom regions in a custom Matlab script. Noise metrics were calculated in a rectangular region outside the

sample. For all ^{1}H and ^{23}Na images, relative signal values of the tissue (Avg_{muscle}) compared to the 5% agarose phantom ($Avg_{gel\ ref\ phantom}$) were acquired, as shown in Eq IV.1. For ^{1}H images T_2W/T_1W average signal ratios were also calculated along with tissue signal heterogeneity (H_{sig}), as shown in Eq IV.2 (64). All calculated NMR indices were plotted relative to age of the tissue samples.

$$Relative_{sig} = \frac{Avg_{muscle}}{Avg_{gel\ ref\ phantom}} \qquad \text{(Eq IV.1)}$$

$$H_{sig} = \sqrt{(SD_{muscle})^2 - \left(\frac{SD_{noise}}{0.665}\right)^2} \qquad \text{(Eq IV.2)}$$

Before analysis, all ^{31}P spectra were normalized by dividing by the volume of each sample, which was measured by fluid-displacement. Spectra were then manually zeroth-order phase-corrected. Phosphocreatine peak integration values were plotted relative to sample age.

IV.4 Results

IV.4.1 T_1 and T_2 of Rectus Femoris Tissue Sample

Approximate ^{1}H T_1 (836 ms) and T_2 (40 ms) values were calculated on a single GRMD RF muscle tissue. T_1 was calculated based on the T_1 recovery curve, where T_1 corresponds to the time it takes for ~63% of the magnetization to recover alignment with B_0 after excitation (31). Similarly, T_2 was calculated on the T_2 decay curve, where T_2 corresponds to the time it takes for the signal amplitude to be reduced by ~36% of its original value after excitation. ^{23}Na T_2 (4.23 ms) value was calculated in the same

manner, as ^{1}H. However, when calculating ^{23}Na T_1, various values of TR ranging from 70 ms to 200 ms did not show much of a difference in signal amplitude, therefore indicating that signal saturation was not occurring because T_1 was lower than the 70 ms. Due to the short T_2 (0.5ms- 5ms) of intracellular sodium, it is likely that the sodium observed is mainly the extracellular portion of total sodium concentration (TSC) (72). T_1 and T_2 curves for ^{1}H, as well as a T_2 curve for ^{23}Na are shown in Figure IV-2.
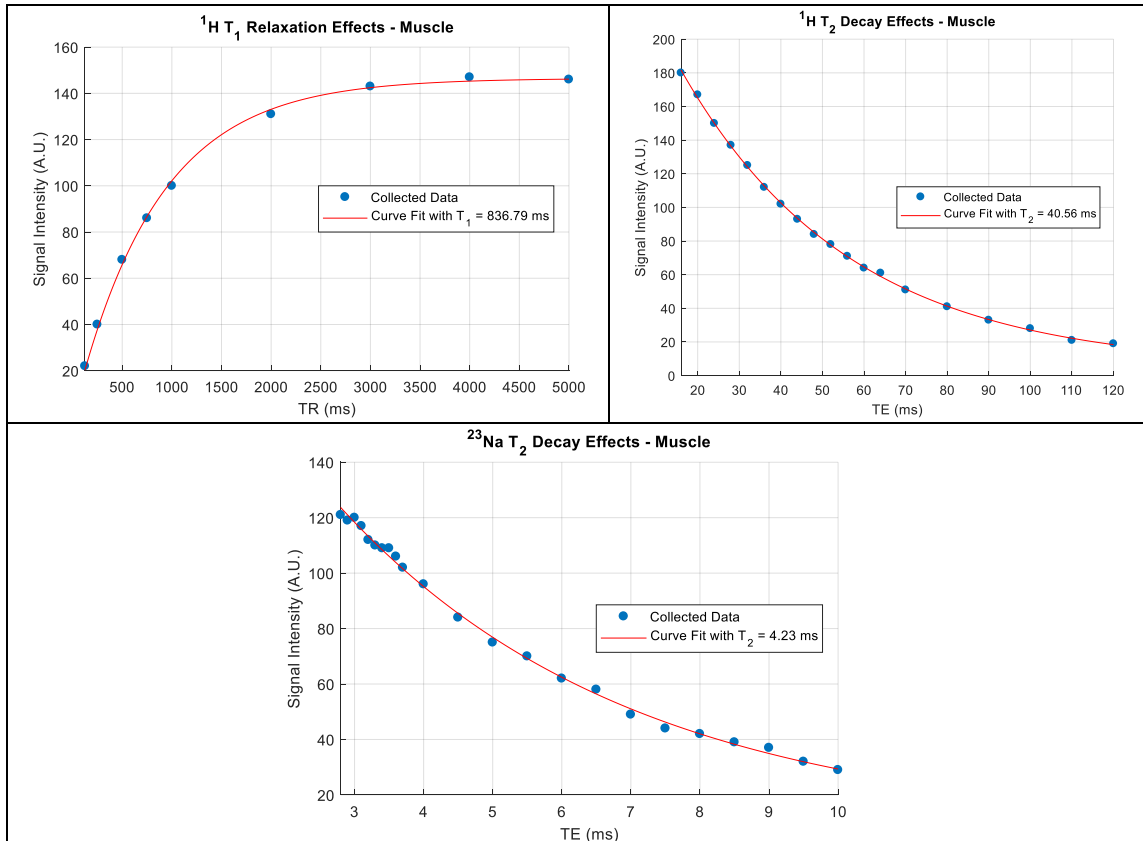
Figure IV-2. ^{1}H T_1 and T_2 curves (top) and ^{23}Na T_2 curve (bottom). T_1 relaxation and T_2 decay curves were plotted over the collected data points. Good curve fits, based on the calculated T_1 and T_2 values, are shown for all plots.

IV.4.2 ^{1}H Imaging

   An example of segmentation of a tissue sample, phantom region, and noise region on ^{1}H T1-weighted and ^{1}H T2-weighted images are shown in Figure IV-3. Segmentation was performed on a center transverse slice of every sample imaged. Each segmented slice was visually inspected to ensure proper regions-of-interest (ROI) were selected before saving all the data for further analysis.
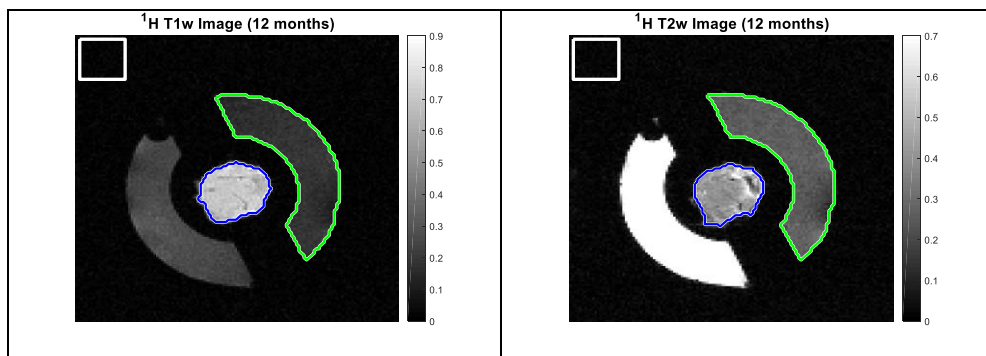
Figure IV-3. Selection of ROIs in a ^{1}H T1-weighted image (left) and ^{1}H T2-weighted image (right). The three ROIs selected were: tissue (blue), gelatinized sodium reference phantom (green), and noise (white).

   Based on the segmented regions and Eq IV.1- Eq IV.2, ^{1}H T1w and T2w relative signal, T1w and T2w heterogeneity, and T2w/T1w relative signal ratio were calculated on a single slice pertaining to each sample. As seen in Figure IV-4A and Figure IV-4B, there was no observable correlation between age and T1w or T2w relative signal, nor between age and T1w and T2w heterogeneity. On the contrary, there was considerable

variation in both T1w and T2w relative signal and heterogeneity, even amongst age-matched samples. If we separate all samples into two groups corresponding to younger (3-6 months) and older (≥12 months) GRMD models, as done by Kornegay et al. (77), a decrease in T2w/T1w signal intensities was noted for the four older GRMD models, as shown in Figure IV-4C.
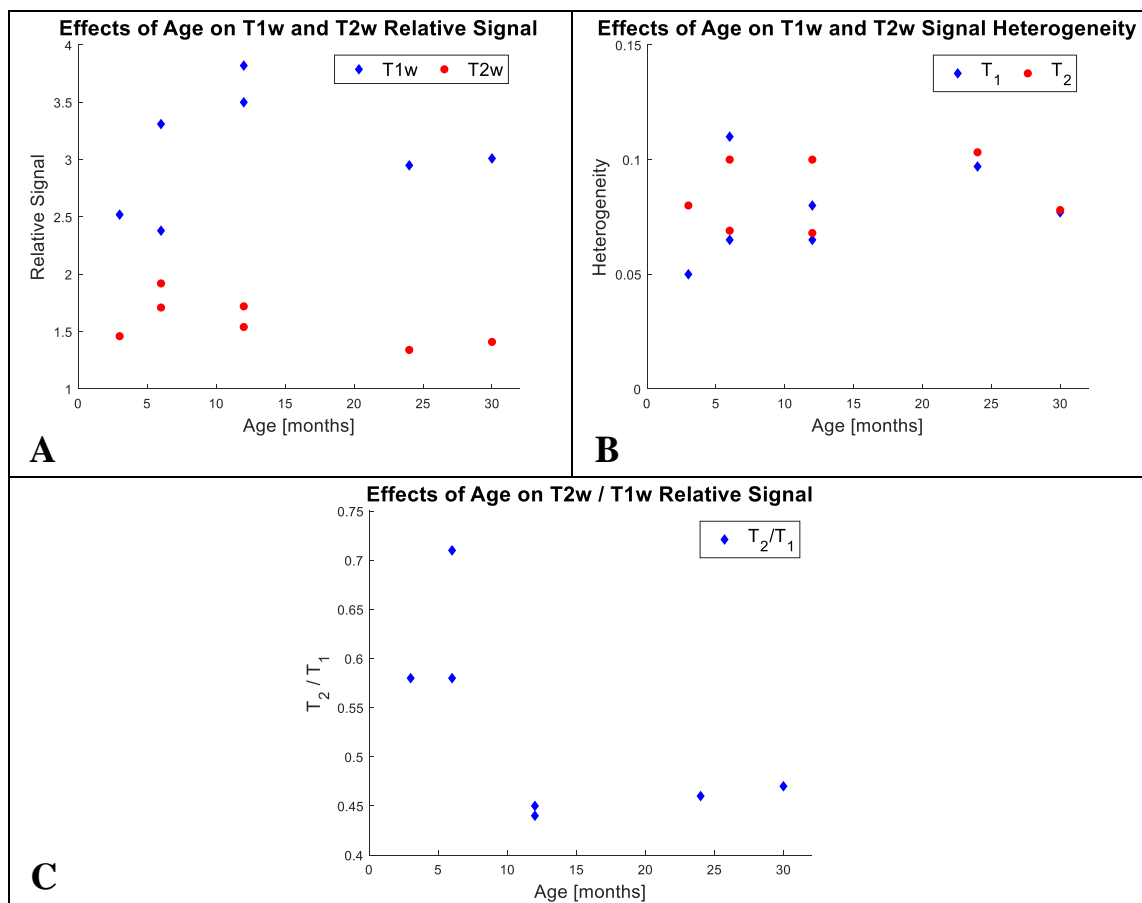
Figure IV-4. Effects of age on selected ^{1}H NMR indices. There was no observable correlation between age and T1w and T2w relative signal, and heterogeneity (A) and (B). However, a decrease in T2w/T1w ratio was observed in the four older GRMD models (C).

IV.4.3 ^{23}Na Imaging

The ^{1}H images acquired with the same resolution as the ^{23}Na images were used to assist in tissue, phantom, and noise segmentation. This was especially for useful ^{23}Na image segmentation, since the achievable SNR of ^{23}Na imaging is much lower than that ^{1}H due to the lower gyromagnetic ratio (approximately a quarter of ^{1}H) and lower biological concentration of sodium (78). As shown in Figure IV-5A and IV-5B, ROIs were first selected on the ^{1}H image then directly applied to the ^{23}Na image, respectively. These segmented regions were then used to analyze the effect of age on ^{23}Na relative signal (^{23}Na signal from tissue / ^{23}Na signal from 50 mM 5% agarose phantom). As shown in Figure IV-5C, there is a large variation in ^{23}Na signal even in age-matched GRMD models. Additionally, there is no observable correlation between age and ^{23}Na relative signal.
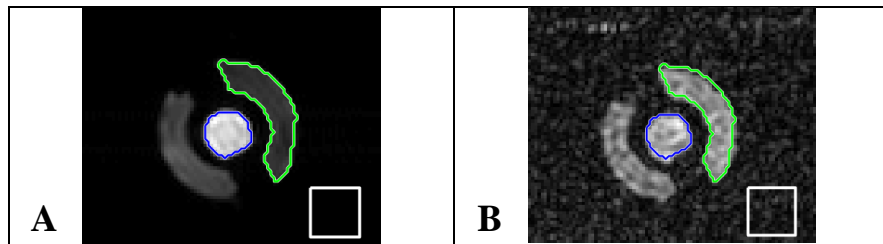
Figure IV-5. Selection of ROIs and effects of age on ^{23}Na relative signal. The selected ROIs (blue- tissue; green- agarose phantom; white- noise) on ^{1}H reference image (left) and ^{23}Na image (right). There was no observable correlation between age and ^{23}Na relative signal.
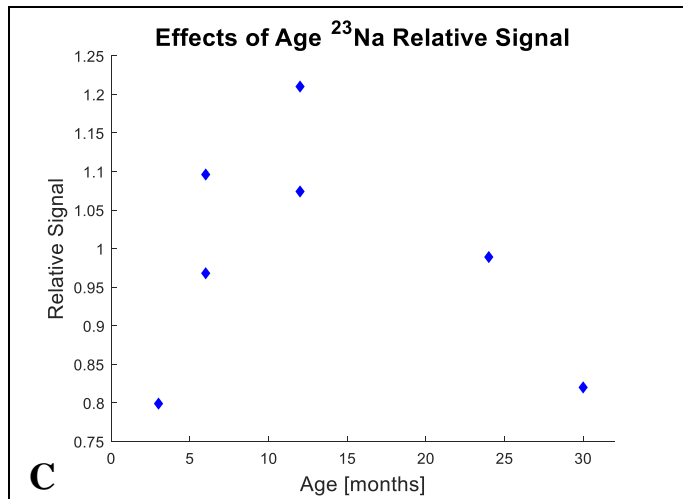
Figure IV-5 Continued.

IV.4.4 ^{31}P Spectroscopy

As shown in the Figure IV-6A, only one peak was observed in the phosphorus

spectra, as expected (76). The chemical shift, relative to the phosphoric acid phantom,

showed that the tissue peak corresponds to phosphocreatine (28,76). Both the peak

height, Figure IV-6A, and peak integration, Figure IV-6B, varied greatly amongst all

samples and showed no observable correlation with age, a contradiction to our previous

work on samples acquired from a different muscle group (76).
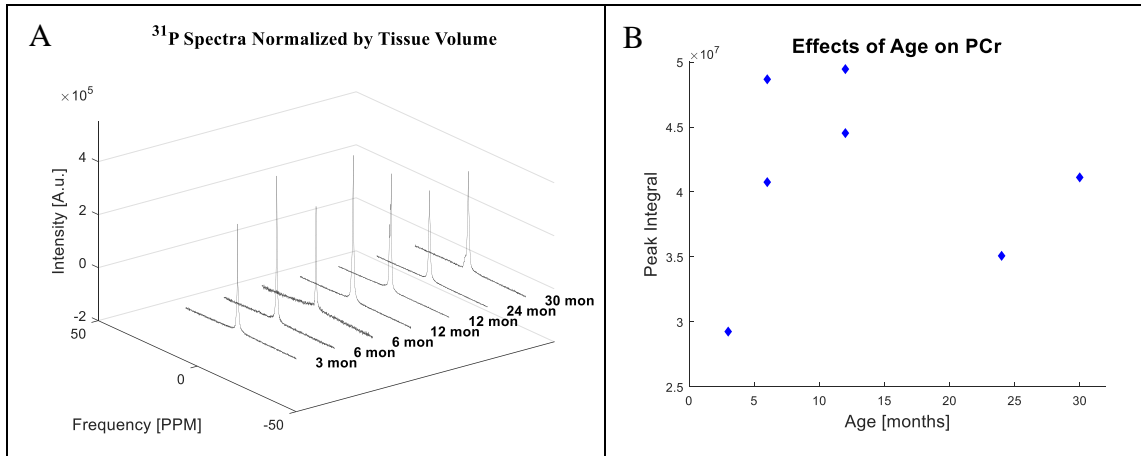
Figure IV-6. Waterfall plot of ^{31}P spectra arranged in order of increasing age (left). Effects of age on PCr signal, as measured by integration under the PCr peak, did not show a notable correlation (right).

IV.4.5 Imaging and Spectroscopy on Samples Excluded from Biomarker Characterization

As previously mentioned, due to significant differences in signal achieved from three tissue samples, only seven tissue samples were used to study the effects of age on selected NMR indices. The affected three samples were all excised and formalin fixed within a couple of weeks from each other, unlike the remaining seven samples. Therefore, it was suspected that the fixation process or sample handling may have affected the achievable signal. Further evaluation on the effects of formalin fixation on skeletal muscle MRI/MRS will be performed. However, that is beyond the scope of this project. Image segmentation on ^{23}Na images, as shown in Figure IV-7, show absence of ^{23}Na within the tissue region for Sample 1, Sample 3, and Sample 4. Additionally,

Figure IV-8 shows low PCr concentrations in Sample 1, Sample 3, and Sample 4 relative

to Sample 8 (based on peak height).

| Sample 1 | Sample 3 | Sample 4 | Sample 8 |
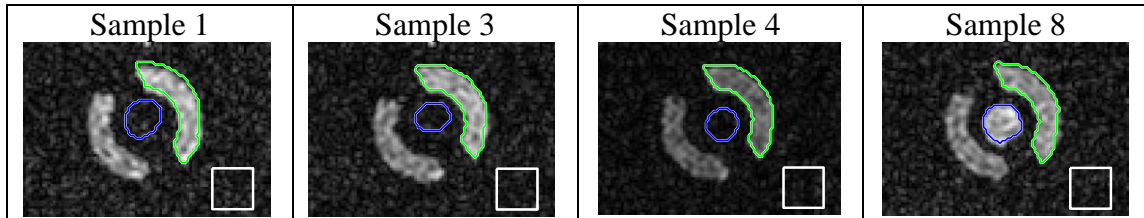
Figure IV-7. Segmented ^{23}Na images of samples with low ^{23}Na concentration. Sample 1 (RS: 0.23), Sample 3 (RS: 0.20), and Sample 4 (RS: 0.22) had a relative signal (RS) approximately six times lower than Sample 8 (RS: 1.21) and four times lower than the lowest ^{23}Na relative signal pertaining to Sample 10.

^{31}P Spectra Normalized by Tissue Volume
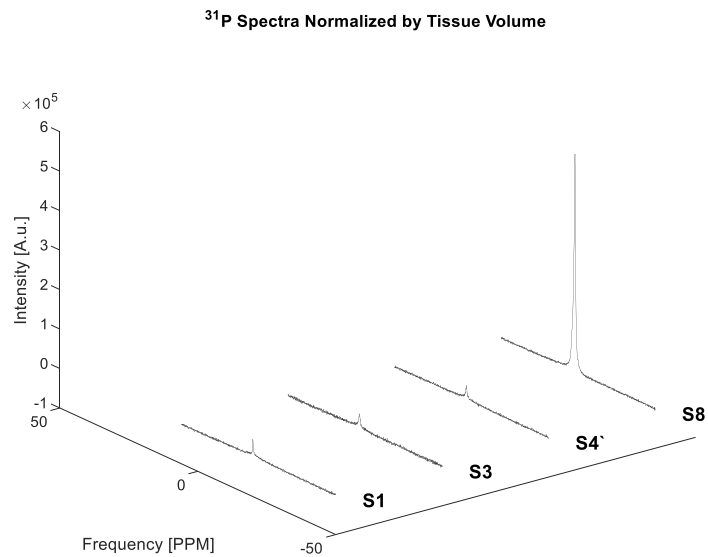
Figure IV-8. ^{31}P waterfall plot of samples with low PCr concentration. Sample 1 (integration: 7.8 e+6), Sample 3 (integration: 8.7 e+6), and Sample 4 (integration: 7.9 e+6) had integration values approximately a order of magnitude lower than that of Sample 8 (9.8 e+7) and seven times lower than the lowest integration value pertaining to Sample 10.

IV.5 Discussion

In this study, notable correlated differences in the NMR indices were not observed amongst the seven age-matched rectus femoris muscles for several possible reasons. This could be attributed to the phenotypic variations in the samples (66,67). This study was also largely limited by the low number of tissue samples, which is common in large animal studies, and lack of age-matched healthy controls. Additionally, previous studies have shown progressive changes in T_1 and T_2 of brain tissue over formalin fixation time (79,80). Therefore, the effects of formalin fixation, if any, should be accounted for when comparing various muscles which were formalin fixed at different time points.

IV.6 Conclusion

Custom RF coils were constructed in order to acquire ^{1}H images, [23]Na images, and ^{31}P spectra to assess rectus femoris muscles from GRMD models of various ages. The NMR indices evaluated did not show any notable observations varying with age in these particular samples. Regardless, the hardware and positioning fixtures developed will allow for straightforward studies in the future of the numerous samples available to our group from this colony. This will allow for future studies to account for phenotypic variations and potential variations caused by prolonged formalin fixation.

CHAPTER V

CONCLUSION AND FUTURE WORK

The work mentioned in this dissertation describes the contribution of hardware advancements, specifically custom RF coils and additional hardware, to enable studies of disease using MR imaging and spectroscopy. The construction of the 32-channel receive array for breast imaging at 7T and the double-tuned birdcage coils for imaging and spectroscopy at 4.7T of GRMD rectus femoris tissue samples enabled studies beyond clinically-standard ^{1}H imaging. Overall, coil characterization on the bench and via imaging/spectroscopy studies showed good coil performance of all constructed RF coils. This section will summarize results found in all the studies reported, potential improvements, and preliminary data pertaining to future works.

V.1 32-Channel Receive Array and Modified FCE Transmit Coil

The bilateral 32-channel receive array and FCE volume coil showed homogenous excitation, significant improvements in SNR, and receive element isolation. Additionally, feasibility of accelerating and acquiring images with high spatial resolution showed the potential utility of the coil for acquiring images with high spatial and temporal resolutions for dynamic studies such as dynamic contrast enhanced MRI and diffusion weighted imaging. Future works include replacement of the receive elements located partially along the z-axis with butterfly surface coils to achieve a more transverse RF field, phantom studies on a heterogeneous phantom with more clinical significance, and of course the use of the array in clinical studies.

V.2 ^{1}H/^{23}Na and ^{1}H/^{31}P Double-Tuned Birdcage Coils

The double-tuned birdcage coils showed coil homogeneity and ability to distinguish between different biological concentrations of ^{23}Na and ^{31}P in various phantoms and rectus femoris tissue samples. Although the NMR indices evaluated did not show any notable observations varying with age in the rectus femoris samples, the hardware and positioning fixtures developed will allow for straightforward studies in the future of the numerous samples available to our group from the GRMD colony. Future works include: studying the effects of formalin fixation and flash-freezing muscle tissue, construction of smaller triple-tuned RF coils to evaluate smaller tissue samples, and construction of a user-friendly graphical user interface for post processing GRMD data. Preliminary data pertaining to future works is described below.

V.2.1 Assessment of Formalin Fixation and Flash-Freezing Muscle Tissue

The studies on the effects of formalin fixation and flash-freezing muscle tissue have been performed on formalin-fixed heart samples excised from the left ventricular wall. However, due to the small size of the samples, shown in Figure V-1, the ^{23}Na images and ^{31}P spectra did not have sufficient SNR to provide valuable results to compare to flash-frozen muscles. Therefore, these studies will continue when small triple-tuned coils are constructed to increase sensitivity to the small samples and streamline the imaging/spectroscopy process, as needed for frozen samples.
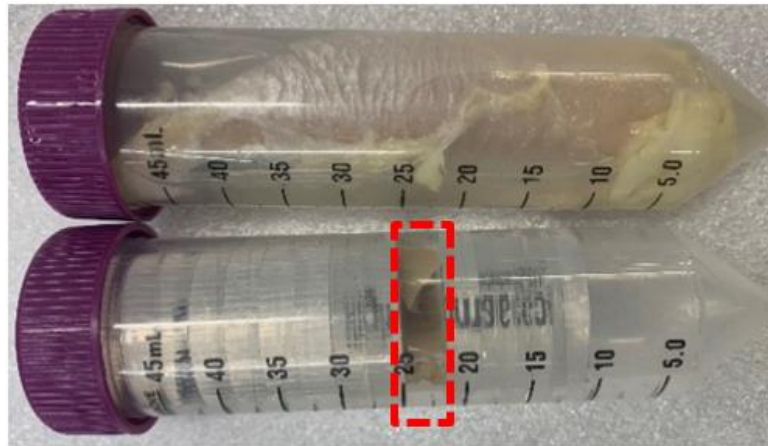
Figure V-1. Size comparison of heart tissue samples and rectus femoris muscle. Pieces of heart tissue were excised from the left ventricular wall of GRMD models. The bottom 50 ml vial shows the heart tissue sample (in red dashed box) placed between acrylic spacers, while the top vial shows a rectus femoris muscle, which almost completely filled the sample vial.

Images and spectra of the formalin-fixed heart muscle of two GRMD models are shown in Figure V-2 and Figure V-3. Due to the large voxel size (5x5x6 mm) necessary for sodium imaging, it is difficult to identify if dark regions within the tissue region are due to spacing between the tissue samples or partial volume effects. Therefore, an increase in SNR is necessary to acquire higher resolution sodium images of these small samples before further analysis.
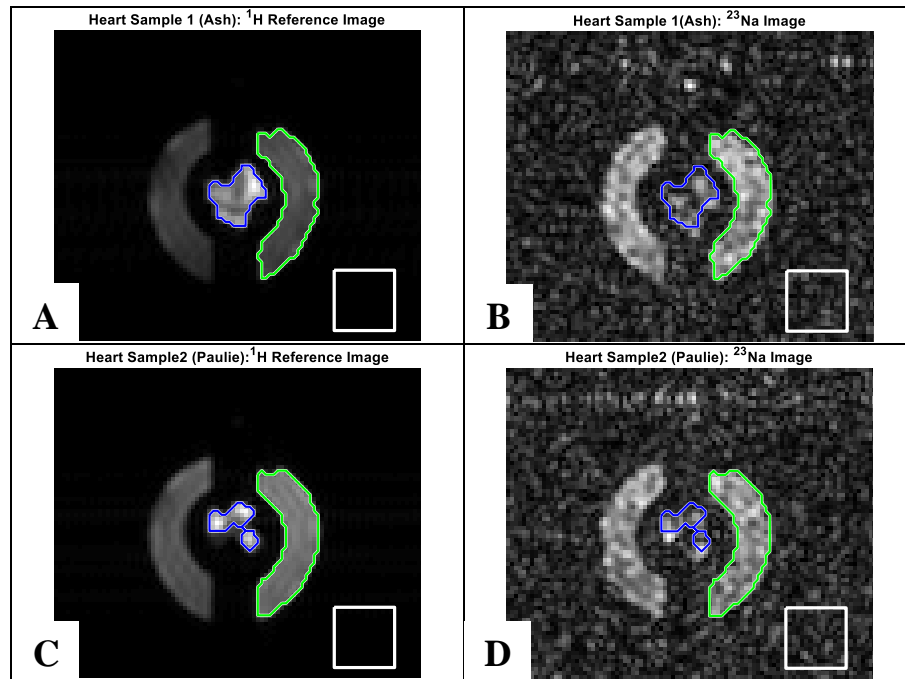
Figure V-2. ^{1}H reference images and ^{23}Na images of two heart samples. Partial volume effects, due to large voxel sizes compared to tissue size, are visible in ^{1}H reference images. Additionally, performing the tissue segmentation on the ^{1}H reference images and applying those tissue boundaries directly to the ^{23}Na images did not work as well with these small tissue samples.

^{31}P spectra of the heart samples did not show a PCr peak on the Varian even after acquiring 500 averages. Therefore, parameters could not be optimized for ^{31}P experiments. However, when plotting the spectra in Matlab, a single PCr peak with low SNR appeared for both samples, as shown in Figure V-3.
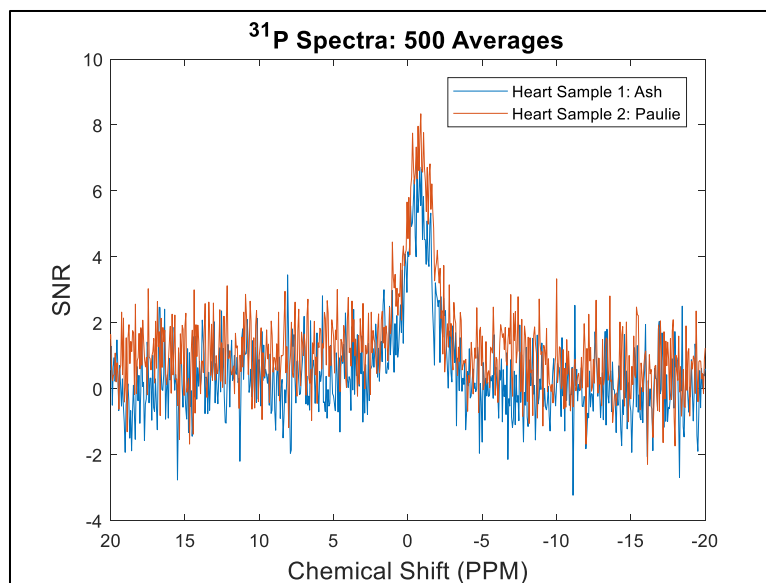
Figure V-3. ^{31}P spectra of both heart samples. Spectra of each sample was acquired with 500 averages. The SNR of each peak was 6.9 and 8.3, respectively. This PCr peak was only visible after post-processing, therefore could not be used to optimize parameters when scanning.

V.2.2 Construction of Triple-Tuned Coils

A three-element triple-tuned array with switchable matching and tuning was constructed in collaboration with colleagues, as shown in Figure V-4 (81). This triple-tuned array for ^{1}H, ^{13}C, and ^{31}P at 3T utilized PIN diodes to switch between different resonant modes. This design demonstrated straight-forward tuning and matching at all three frequencies. However, a loss in Q of the coils was observed and was mainly attributed to the switching mechanism; therefore calling for further coil optimizations.
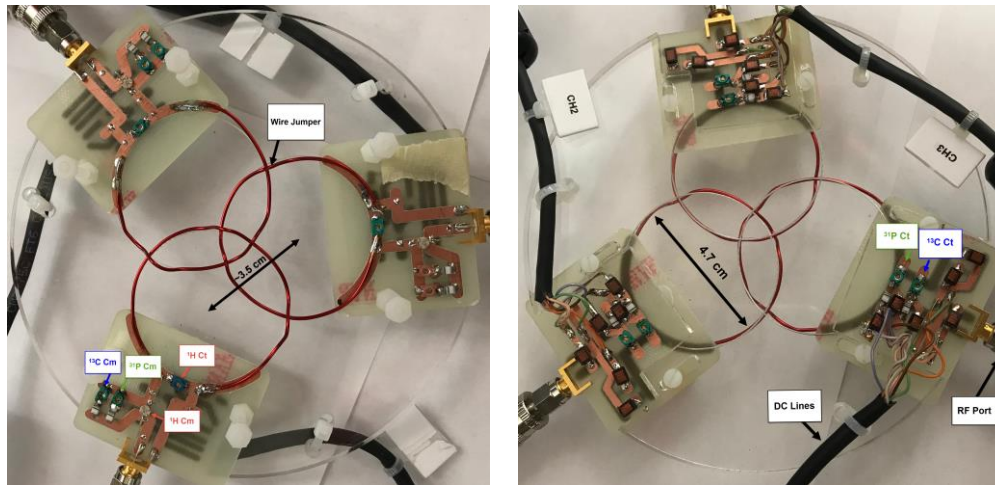
Figure V-4. Top and bottom views of the triple-tuned switchable array. The top view of the array (left) shows the variable matching and tuning capacitors for the ^{1}H frequency, and the variable match capacitors and PIN diodes for the 31P frequency and the ^{13}C frequency. The bottom view of the array (right) shows the variable tuning capacitors and PIN diodes for the ^{31}P frequency and the ^{13}C frequency, all the RF chokes and DC lines for the switching network, and the RF port for each element.

V.2.3 User-Friendly GUI for GRMD Data

Currently, separate Matlab scripts are used to process all GRMD data; with three main scripts used to assess the three nuclei of interest. Each main script calls out functions which perform: segmentation of various regions, SNR measurements, relative signal measurements, signal heterogeneity etc. Although this works well on the data acquired, it would be beneficial to have one collective script with a user-friendly GUI for processing multiple datasets.

REFERENCES

1.   Lauterbur PC. Image Formation by Induced Local Interactions: Examples
        Employing Nuclear Magnetic Resonance. *Nature*. 1973. doi:10.1038/242190a0.

2.   Mansfield P, Grannell P. NMR 'diffraction' in solids? *J. Phys. C: Solid State
        Phys.* 2001. doi:10.1088/0022-3719/6/22/007

3.   Cancer Stat Facts: Female Breast Cancer. National Cancer Institute: Surveillance,
        Epidemiology, and End Results Program Web site.
        https://seer.cancer.gov/statfacts/html/breast.html. Accessed September 2019.

4.   Kuhl CK. The Changing World of Breast Cancer: A Radiologist's Perspective.
        Invest radiol. 2015. doi:10.1097/RLI.0000000000000166.

5.   Bartella L, Smith CS, Dershaw DD, Liberman L. Imaging Breast Cancer. *Radiol
        Clin North Am.* 2007. doi:10.1016/j.rcl.2006.10.007.

6.   Kriege M, Brekelmans CT, Boetes C, Besnard PE, Zonderland HM, Obdeijn IM,
        Manoliu RA, Kok T, Peterse H, Tilanus-Linthorst MM, Muller SH, Meijer S,
        Oosterwijk JC, Beex LV, Tollenaar RA, de Koning H, Rutgers EJ, Klijn JG.
        Efficacy of MRI and Mammography for Breast-Cancer Screening in Women
        with a Familial or Genetic Predisposition. *N Engl J Med.* 2004. doi:
        10.1056/NEJMoa031759

7.   Berg WA, Gutierrez L, NessAiver MS, Carter WB, Bhargavan M, Lewis RS,
        Ioffe OB. Diagnostic accuracy of mammography, clinical examination, US, and
        MR imaging in preoperative assessment of breast cancer. *Radiology*. 2004.
        doi:10.1148/radiol.2333031484

8.   Kuhl CK, Schrading S, Leutner CC, Morakkabati-Spitz N, Wardelmann E,
        Fimmers R, Kuhn W, Schild HH. Mammography, breast ultrasound, and
        magnetic resonance imaging for surveillance of women at high familial risk for
        breast cancer. *Journal of Clin Oncol*. 2005. doi:10.1200/JCO.2004.00.4960.

9.   Youssef MA, Elahwal HMS, Alwageeh MM, Attya SE. Role of MRI in
        differentiating benign from malignant breast lesions using dynamic contrast
        enhanced MRI and diffusion weighted MRI. *Alexandria Med J.* 2018.
        doi:10.1016/j.ajme.2016.12.008.

10.   Tan SL, Rahmat K, Rozalli FI, Mohd-Shah MN, Aziz YF, Yip CH,
        Vijayananthan A, Ng KH. Differentiation between benign and malignant breast
        lesions using quantitative diffusion-weighted sequence on 3 T MRI. *Clin Radiol.*
        2014. doi:10.1016/j.crad.2013.08.007.

11.   Partridge SC, Rahbar H, Murthy R, Chai X, Kurland BF, DeMartini WB, Lehman CD. Improved diagnostic accuracy of breast MRI through combined apparent diffusion coefficients and dynamic contrast-enhanced kinetics. *Magn Reson Med.* 2011. doi:10.1002/mrm.22762

12.   Kuhl CK, Mielcareck P, Klaschik S, Leutner C, Wardelmann E, Gieseke J, Schild H. Dynamic Breast MR Imaging: Are Signal Intensity Time Course Data Useful for Differential Diagnosis of Enhancing Lesions? *Radiology* 1999. doi:10.10.1148/radiology.211.1.r99ap38101.

13.   Yabuuchi H, Matsuo Y, Okafuji T, Kamitani T, Soeda H, Setoguchi T, Sakai S, Hatakenaka M, Kubo M, Sadanaga N, Yamamoto H, Honda H. Enhanced mass on contrast-enhanced breast MR imaging: Lesion characterization using combination of dynamic contrast-enhanced and diffusion-weighted MR images. *J Magn Reson Imaging*. 2008. doi:10.1002/jmri.21570.

14.   Kim J, Santini T, Bae KT, Krishnamurthy N, Zhao Y, Zhao T, Ibrahim TS. Development of a 7 T RF coil system for breast imaging. *NMR Biomed.* 2017. doi:10.1002/nbm.3664.

15.   Brown R, Storey P, Geppert C, McGorty K, Leite APK, Babb J, Sodickson DK, Wiggins GC, Moy L. Breast MRI at 7 Tesla with a bilateral coil and T1-weighted acquisition with robust fat suppression: image evaluation and comparison with 3 Tesla. *Eur Radiol.* 2013. doi: 10.1007/s00330-013-2972-1.

16.   Voogt IJ, van de Bank BL, Luijten PR, Klomp DW, Italiaander M, and Roon R. 30 channel unilateral breast coil for ultra high resolution MRI at 7T. In Proceedings of the 19th Annual Meeting of ISMRM, Montreal, Quebec, Canada, 2011. p.3818

17.   Italiaander M, Voogt IJ, Kalleveen I, Stehouwer B, Velde T, Luijten P, Boer V, and Klomp D. Uniform bilateral breast MRI at 7T with dual transmit and 30-channel receive. In Proceedings of the 21st Annual Meeting of ISMRM, Salt Lake City, Utah, USA, 2013. p.2729

18.   Krikken E, Steensma BR, Voogt IJ, Luijten PR, Klomp DWJ, Raaijmakers AJE, Wijnen JP. Homogeneous B1+ for bilateral breast imaging at 7 T using a five dipole transmit array merged with a high density receive loop array. *NMR Biomed*. 2019. doi:10.1002/nbm.4039.

19.   Szigyarto CA-K, Spitali P. Biomarkers of Duchenne muscular dystrophy: current findings. *Degener Neurol Neuromuscul Dis.* 2018. doi:10.2147/DNND.S121099.

20.   Wary C, Azzabou N, Giraudeau C, Le Louer J, Montus M, Voit T, Servais L, Carlier P. Quantitative NMRI and NMRS identify augmented disease progression after loss of ambulation in forearms of boys with Duchenne muscular dystrophy. *NMR Biomed.* 2015. doi:10.1002/nbm.3352.

21.   Barnard AM, Willcocks RJ, Finanger EL, Daniels MJ, Triplett WT, Rooney WD, Lott DJ, Forbes SC, Wang DJ, Senesac CR, Harrington AT, Finkel RS, Russman BS, Byrne BJ, Tennekoon GI, Walter GA, Sweeney HL, Vandenborne K. Skeletal muscle magnetic resonance biomarkers correlate with function and sentinel events in Duchenne muscular dystrophy. *PLoS One.* 2018. doi: 10.1371/journal.pone.0194283.

22.   Willcocks RJ, Rooney WD, Triplett WT, Forbes SC, Lott DJ, Senesac CR, Daniels MJ, Wang DJ, Harrington AT, Tennekoon GI, Russman BS, Finanger EL, Byrne BJ, Finkel RS, Walter GA, Sweeney HL, Vandenborne K. Multicenter prospective longitudinal study of magnetic resonance biomarkers in a large duchenne muscular dystrophy cohort. *Annals of neurology.* 2016. doi:10.1002/ana.24599.

23.   Finanger EL, Russman B, Forbes SC, Rooney WD, Walter GA, Vandenborne K. Use of skeletal muscle MRI in diagnosis and monitoring disease progression in Duchenne muscular dystrophy. *Phys Med Rehabi Clin N Am.* 2012. doi: 10.1016/j.pmr.2011.11.004.

24.   Kinali M, Arechavala-Gomeza V, Cirak S, Glover A, Guglieri M, Feng L, Hollingsworth KG, Hunt D, Jungbluth H, Roper HP, Quinlivan RM, Gosalakkal JA, Jayawant S, Nadeau A, Hughes-Carre L, Manzur AY, Mercuri E, Morgan JE, Straub V, Bushby K, Sewry C, Rutherford M, Muntoni F. Muscle histology vs MRI in Duchenne muscular dystrophy. *Neurology*. 2011. doi: 10.1212/WNL.0b013e318208811f.

25.   Weber MA, Nagel AM, Jurkat-Rott K, Lehmann-Horn F. Sodium (23Na) MRI detects elevated muscular sodium concentration in Duchenne muscular dystrophy. *Neurology.* 2011. doi: 10.1212/WNL.0b013e31823b9c78.

26.   Gerhalter T, Gast LV, Marty B, Martin J, Trollmann R, Schüssler S, Roemer F, Laun FB, Uder M, Schröder R, Carlier PG, Nagel AM. 23Na MRI depicts early changes in ion homeostasis in skeletal muscle tissue of patients with duchenne muscular dystrophy. *J Magn Reson Imaging.* 2019. doi:10.1002/jmri.26681.

27.   Weber MA, Nagel AM, Wolf MB, Jurkat-Rott K, Kauczor HU, Semmler W, Lehmann-Horn F. Permanent muscular sodium overload and persistent muscle

edema in Duchenne muscular dystrophy: a possible contributor of progressive muscle degeneration. *J Neurol.* 2012. doi:10.1007/s00415-012-6512-8.

28.   Wary C, Naulet T, Thibaud JL, Monnet A, Blot S, Carlier PG. Splitting of Pi and other 31P NMR anomalies of skeletal muscle metabolites in canine muscular dystrophy. *NMR Biomed.* 2012. doi:10.1002/nbm.2785.

29.   Hooijmans MT, Doorenweerd N, Baligand C, Verschuuren J, Ronen I, Niks EH, Webb AG, Kan HE. Spatially localized phosphorous metabolism of skeletal muscle in Duchenne muscular dystrophy patients: 24-month follow-up. *PLoS One.* 2017. doi:10.1371/journal.pone.0182086.

30.   McCully K, Giger U, Argov Z, Valentine B, Cooper B, Chance B, Bank W. Canine X-linked muscular dystrophy studied with in vivo phosphorus magnetic resonance spectroscopy. *Muscle & nerve.* 1991. doi:10.1002/mus.880141109.

31.   NessAiver M. All You Really Need to Know about MRI Physics. Baltimore, Maryland: Simply Physics; 1997. 140 p.

32.   Ackerman JJ, Grove TH, Wong GG, Gadian DG, Radda GK. Mapping of metabolites in whole animals by 31P NMR using surface coils. *Nature.* 1980. doi:10.1038/283167a0.

33.   Wright SM , Wald LL. Theory and application of array coils in MR spectroscopy. *NMR Biomed.* 1997. doi:10.1002/(SICI)1099-1492(199712)10:8<394::AID-NBM494>3.0.CO;2-0.

34.   Gruber B, Froeling M, Leiner T, Klomp DWJ. RF coils: A practical guide for nonphysicists. *J Magn Reson Imaging.* 2018. doi:10.1002/jmri.26187.

35.   Hoult DI, Lauterbur PC. The sensitivity of the zeugmatographic experiment involving human samples. *J Magn Reson (1969).* 1979. doi:10.1016/0022-2364(79)90019-2.

36.   Hoult DI, Richards RE. The signal-to-noise ratio of the nuclear magnetic resonance experiment. *J Magn Reson (1969).* 1976. doi: 10.1016/0022-2364(76)90233-X.

37.   Cui J, Del Bosque R, Dimitrov I, Cheshkov S, McDougall MP, Malloy C, Wright SM. Modified Forced Current Excitation Transmit Coil with Receive Array Insert for Bilateral Imaging at 7T. In Proceedings of the 25th Annual Meeting of ISMRM, Honolulu, HI, USA, 2017. p.2706

38.   By S, Cheshkov S, Dimitrov I, Cui J, Seiler S, Goudreau S, Malloy C, Wright S, McDougall M, Kinner S. A 16-Channel Receive, Forced Current Excitation Dual-Transmit Coil for Breast Imaging at 7T. *PLoS One*. 2014. doi:10.1371/journal.pone.0113969.

39.   Fowler AM, Mankoff DA, Joe BN. Imaging Neoadjuvant Therapy Response in Breast Cancer. *Radiology.* 2017. doi:10.1148/radiol.2017170180.

40.   Stehouwer BL, Klomp DW, van den Bosch MA, Korteweg MA, Gilhuijs KG, Witkamp AJ, van Diest PJ, Houwert KA, van der Kemp WJ, Luijten PR, Mali WP, Veldhuis WB. Dynamic contrast-enhanced and ultra-high-resolution breast MRI at 7.0 Tesla. *Eur Radiol*. 2013. doi:10.1007/s00330-013-2985-9.

41.   Menezes GLG, Stehouwer BL, Klomp DWJ, van der Velden TA, van den Bosch MAAJ, Knuttel FM, Boer VO, van der Kemp WJM, Luijten PR, Veldhuis WB. Dynamic contrast-enhanced breast MRI at 7T and 3T: an intra-individual comparison study. *Springerplus.* 2016. doi:10.1186/s40064-015-1654-7.

42.   Pinker K, Bogner W, Baltzer P, Trattnig S, Gruber S, Abeyakoon O, Bernathova M, Zaric O, Dubsky P, Bago-Horvath Z, Weber M, Leithner D, Helbich TH. Clinical application of bilateral high temporal and spatial resolution dynamic contrast-enhanced magnetic resonance imaging of the breast at 7 T. *Eur Radiol.* 2014. doi:10.1007/s00330-013-3075-8.

43.   Bogner W, Pinker K, Zaric O, Baltzer P, Minarikova L, Porter D, Bago-Horvath Z, Dubsky P, Helbich TH, Trattnig S, Gruber S. Bilateral diffusion-weighted MR imaging of breast tumors with submillimeter resolution using readout-segmented echo-planar imaging at 7 T. *Radiology.* 2015. doi:10.1148/radiol.14132340.

44.   van de Bank BL, Voogt IJ, Italiaander M, Stehouwer BL, Boer VO, Luijten PR, Klomp DWJ. Ultra high spatial and temporal resolution breast imaging at 7T. *NMR Biomed.* 2013. doi:10.1002/nbm.2868.

45.   Brown R, Storey P, Geppert C, McGorty K, Klautau Leite AP, Babb J, Sodickson DK, Wiggins GC, Moy L. Breast MRI at 7 Tesla with a bilateral coil and robust fat suppression. *J Magn Reson Imaging.* 2014. doi:10.1002/jmri.24205.

46.   Ladd ME, Bachert P, Meyerspeer M, Moser E, Nagel AM, Norris DG, Schmitter S, Speck O, Straub S, Zaiss M. Pros and cons of ultra-high-field MRI/MRS for human application. *Prog Nucl Magn Reson Spectrosc.* 2018. doi:10.1016/j.pnmrs.2018.06.001.

47.   Fiedler TM, Ladd ME, Bitz AK. SAR Simulations & Safety. *NeuroImage.* 2018. doi:10.1016/j.neuroimage.2017.03.035.

48. McDougall MP, Cheshkov S, Rispoli J, Malloy C, Dimitrov I, Wright SM. Quadrature transmit coil for breast imaging at 7 tesla using forced current excitation for improved homogeneity. *J Magn Reson Imaging.* 2014. doi:10.1002/jmri.24473.

49. Cui J, Rispoli J, Dimitrov I, Cheshkov S, McDougall MP, Malloy C, Wright SM. A Switched-Mode Breast Coil for 7 T MRI Using Forced-Current Excitation. *IEEE Trans Biomed Eng.* 2015. doi:10.1109/TBME.2015.2403850.

50. Cui J, Del Bosque R, Dimitrov I, Cheshkov S, McDougall MP, Malloy C, Wright SM. Modified Forced Current Excitation Transmit Coil with Receive Array Insert for Bilateral Imaging at 7T. In Proceedings of the 25th Annual Meeting of ISMRM, Honolulu, HI, USA, 2017. p.2706

51. Rispoli JV, Wilcox MD, By S, Wright SM, McDougall MP. Effects of coplanar shielding for high field MRI. *Conf Proc IEEE Eng Med Biol Soc*. 2016. doi:10.1109/EMBC.2016.7592157.

52. Wiggins GC , Triantafyllou C, Potthast A, Reykowski A, Nittka M, Wald LL. 32-channel 3 Tesla receive-only phased-array head coil with soccer-ball element geometry. *Magn Reson Med.* 2017. doi:10.1002/mrm.20925.

53. McGhee D, Steele JR. Breast volume and bra size. *Int J Cloth Sci Tech*. 2011. doi: 10.1108/09556221111166284.

54. Reykowski A, Wright SM, Porter JR. Design of Matching Networks for Low Noise Preamplifiers. *Magn Reson Med.* 1995. doi: 10.1002/mrm.1910330617.

55. Seeber DA, Jevtic J, Menon A. Floating shield current suppression trap. *Concepts Magn Reson.* 2004.

56. Del Bosque R, McDougall M. A 16-Channel Mock Receiver Interface Box for MR Array Coil Design. In Proceedings of BMES Annual Meeting, Atlanta , GA, USA, 2018.

57. Microsemi Corp. The PIN Diode Circuit Designers' Handbook. 1998.

58. Bolan PJ, Garwood M, Rosen MA, Levering A, Blume JD, Gimpel J, Esserman J, Hylton N. Design of Quality Control Measures for a Multi-site Clinical Trail of Breast MRS - ACRIN 6657. In Proceedings of the 16th Annual Meeting of ISMRM, Toronto, ON, CA, 2008. p.1588.

59.   Henkelman RM. Measurement of signal intensities in the presence of noise in MR images. *Med Phys.* 1985. doi:10.1118/1.595711.

60.   Wiesinger F, Van de Moortele P-F, Adriany G, De Zanche N, Ugurbil K, Pruessmann KP. Parallel imaging performance as a function of field strength—An experimental investigation using electrodynamic scaling. *Magn Reson Med.* 2004. doi:10.1002/mrm.20281.

61.   Emery AEH. Population frequencies of inherited neuromuscular diseases—A world survey. *Neuromuscul Disord.* 1991. doi:10.1016/09608966(91)90039-u.

62.   Mendell JR, Shilling C, Leslie ND, Flanigan KM, al-Dahhak R, Gastier-Foster J, Kneile K, Dunn DM, Duval B, Aoyagi A, Hamil C, Mahmoud M, Roush K, Bird L, Rankin C, Lilly H, Street N, Chandrasekar R, Weiss RB. Evidence-based path to newborn screening for Duchenne muscular dystrophy. *Ann Neurol.* 2012. doi:10.1002/ana.23528.

63.   Hoffman EP, Brown RH, Kunkel LM. Dystrophin: the protein product of the Duchenne muscular dystrophy locus. *Cell.* 1987. di:10.1016/00928678(87)90579-4.

64.   Thibaud JL, Azzabou N, Barthelemy I, Fleury S, Cabrol L, Blot S, Carlier PG. Comprehensive longitudinal characterization of canine muscular dystrophy by serial NMR imaging of GRMD dogs. *Neuromuscul Disord.* 2012. doi:10.1016/j.nmd.2012.05.010.

65.   Thibaud JL, Monnet A, Bertoldi D, Barthelemy I, Blot S, Carlier PG. Characterization of dystrophic muscle in golden retriever muscular dystrophy dogs by nuclear magnetic resonance imaging. *Neuromuscul Disord.* 2007. doi:10.1016/j.nmd.2007.03.013.

66.   Kornegay JN, Bogan JR, Bogan DJ, Childers MK, Li J, Nghiem P, Detwiler DA, Larsen CA, Grange RW, Bhavaraju-Sanka RK, Tou S, Keene BP, Howard JF, Wang J, Fan Z, Schatzberg SJ, Styner MA, Flanigan KM, Xiao X, Hoffman EP. Canine models of Duchenne muscular dystrophy and their use in therapeutic strategies. *Mamm genome.* 2012. doi:10.1007/s00335-011-9382-y.

67.   Ambrósio CE, Valadares MC, Zucconi E, Cabral R, Pearson PL, Gaiad TP, Canovas M, Vainzof M, Miglino MA, Zatz M. Ringo, a Golden Retriever Muscular Dystrophy (GRMD) dog with absent dystrophin but normal strength. *Neuromuscul Disord.* 2008. doi:10.1016/j.nmd.2008.06.385.

68. Murphy-Boesch J, Srinivasan R, Carvajal L, Brown TR. Two configurations of the four-ring birdcage coil for 1H imaging and 1H-decoupled 31P spectroscopy of the human head. *J Magn Resonan.* 1994. doi:10.1006/jmrb.1994.1017.

69. Chin CL, Collins CM, Li S, Dardzinski BJ, Smith MB. BirdcageBuilder: Design of Specified-Geometry Birdcage Coils with Desired Current Pattern and Resonant Frequency. *Concepts Magn Reson* 2002. doi:10.1002/cmr.10030.

70. Wilcox M, Wright S, McDougall M. Multi-Tuned Cable Traps for Multinuclear MRI and MRS. *IEEE Trans Biomed Eng.* 2019. doi:10.1109/TBME.2019.2933733.

71. Kemp GJ, Meyerspeer M, Moser E. Absolute quantification of phosphorus metabolite concentrations in human muscle in vivo by 31P MRS: a quantitative review. *NMR Biomed.* 2007. doi:10.1002/nbm.1192.

72. Madelin G, Regatte RR. Biomedical applications of sodium MRI in vivo. *J Magn Reson Imaging.* 2013. doi:10.1002/jmri.24168.

73. Doty FD, Connick TJ, Ni XZ, Clingan MN. Noise in high-power, high-frequency double-tuned probes. *J Magn Reson (1969).* 1988. doi:10.1016/0022-2364(88)90011-X.

74. Edwards RH, Dawson MJ, Wilkie DR, Gordon RE, Shaw D. Clinical use of nuclear magnetic resonance in the investigation of myopathy. *Lancet.* 1982. doi:10.1016/s0140-6736(82)92635-6.

75. Sia J. Development of a 1H/31P Spectroscopy Coil Customized for Canine Models of Muscular Dystrophy [Masters Thesis]. College Station, TX: Texas A&M University; 2016.

76. Eresen A, Alic L, Birch SM, Friedeck W, Griffin JF 4th, Kornegay JN, Ji JX. Texture as an imaging biomarker for disease severity in golden retriever muscular dystrophy. *Muscle Nerve.* 2019. doi:10.1002/mus.26386.

77. Bangerter NK, Kaggie JD, Taylor MD, Hadley JR. Sodium MRI radiofrequency coils for body imaging. *NMR Biomed.* 2016. doi:10.1002/nbm.3392.

78. Shepherd TM, Thelwall PE, Stanisz GJ, Blackband SJ. Aldehyde fixative solutions alter the water relaxation and diffusion properties of nervous tissue. *Magn Reson Med.* 2009. doi:10.1002/mrm.21977.

79. Shatil AS, Uddin MN, Matsuda KM, Figley CR. Quantitative Ex Vivo MRI Changes due to Progressive Formalin Fixation in Whole Human Brain

Specimens: Longitudinal Characterization of Diffusion, Relaxometry, and Myelin Water Fraction Measurements at 3T. *Front Med (Lausanne).* 2018. doi:10.3389/fmed.2018.00031.

81. Carrell T, Del Bosque R, Wilcox M, McDougall MP. A Three- Element Triple-Tuned Array Implemented with Switchable Matching and Tuning. In Proceedings of the 27th Annual Meeting of ISMRM, Montreal, QC, CA, 2019. p.1572.

APPENDIX A

TROUBLESHOOTING OF 32-CHANNEL RECEIVE ARRAY COIL

Volume coil T/R images were acquired when all 32- channels were connected

and detuned. A faulty channel showed an intermittent error. Elevated signal in the

volume coil image, shown in Figure A-1, showed that the faulty channel was on the right

side of the bilateral coil. Coil elements were disconnected from the Phillips interface box

four at a time. Open interface channels were terminated with 50 Ω loads before running

the next scan. This was performed until the faulty coil element was narrowed down to

receive element 31.
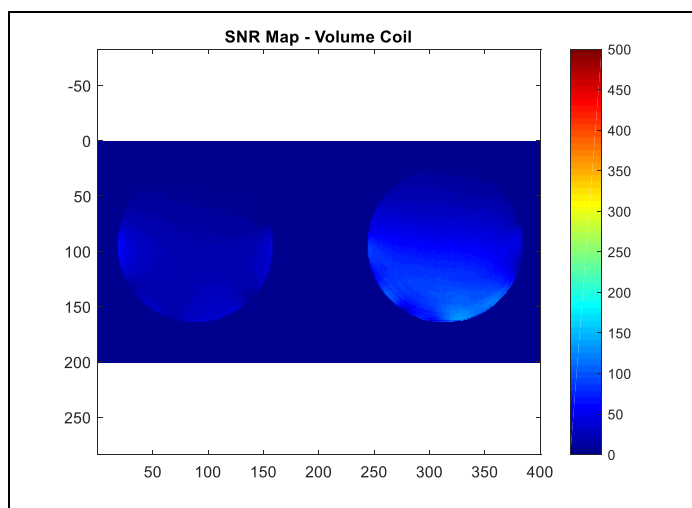
Figure A-1. Volume coil image with faulty receive element on the right side.

The receive element 31 detachable board was then replaced and images were reacquired. This time, the scanner did not display an error, meaning the faulty channel was fixed. However, notable nulls were present along the periphery of both phantoms in the volume coil image and the array image, as shown in Figure A-2. This image pattern had been previously observed when testing the unilateral 16-channel array prior to adding the passive detuning traps. Therefore, the design of the passive detuning traps as well as components chosen were compared between both coils. After looking into the specs of our components, we concluded that the switching speed of the diodes (MA COM, MADP-000235-10720T) on the passive detuning trap may not have been fast enough for this application (298MHz). Therefore, all the diodes were replaced on the 32-element array with the fast-switching diodes which were previously used for this application (Microsemi, UM9989).
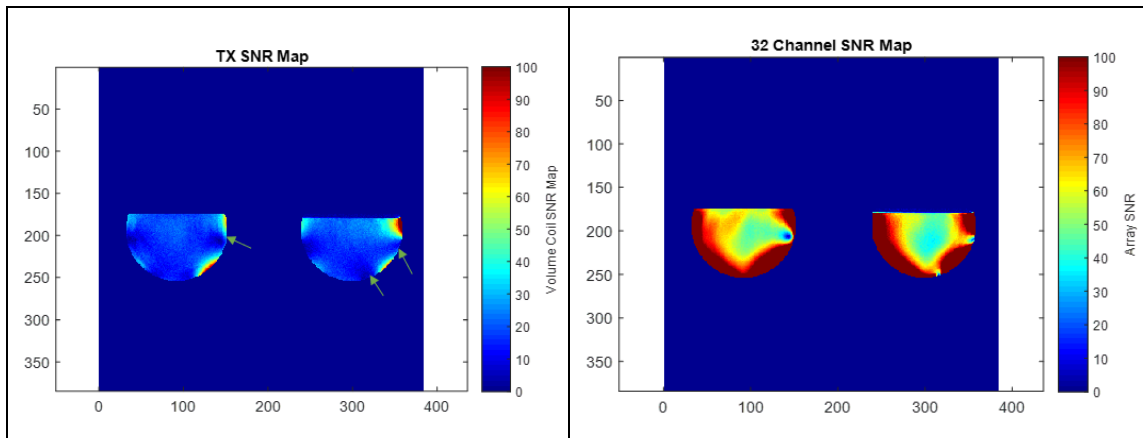
Figure A-2. Volume coil image (left) and array coil image (right) with MA COM diodes on passive detuning traps. Notable nulls along the periphery of both images were observed.

107

Prior to acquiring more images, the 32-channel fan-out board was modified to have an acrylic casing to allow insertion into the magnet bore. This was done to test if the active detuning signal provided by the Philips interface box was sufficient to detune all 32 receive elements during transmit. First, 8 receive channels were connected to the interface box, while the remaining 24 were statically detuned using the fan-out board. Figure A-3 shows the image acquired with 8 receive elements, as well as the volume coil image.
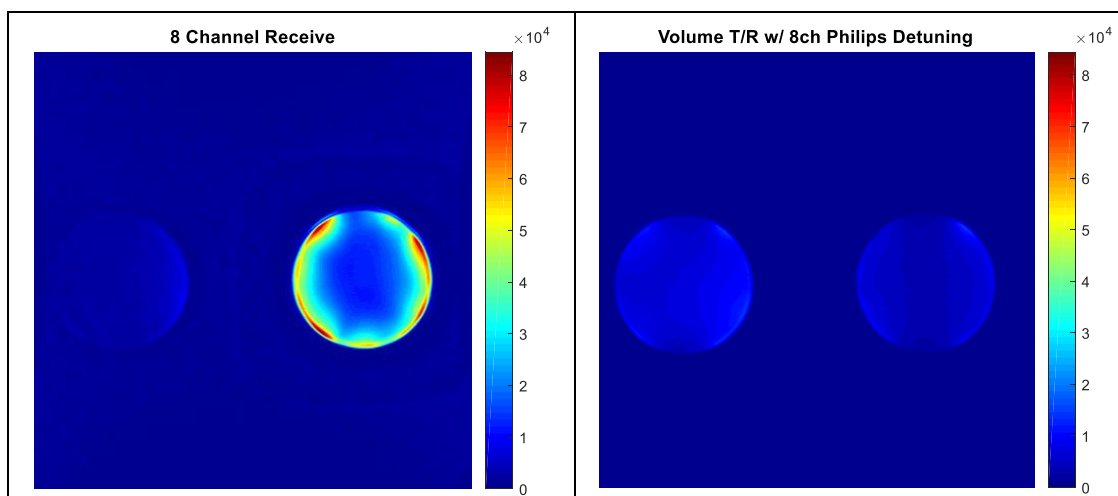

Figure A-3. Array coil image (left) and volume coil image (right) when 8 receive channels were connected to the Philips interface box and 24 were statically detuned using the fan-out board.

This experiment was repeated with 16 receive elements connected to the interface box and 16 statically detuned using the fan-out board. Finally, all 32 channels

were connected to the interface box and a 32-channel image and volume coil image were acquired. These experiments showed an increase in signal along the periphery in the array coil images and homogenous volume coil images. Indicating that the detuning signal provided by the Philips interface box was sufficient to actively detune all 32 receive elements during transmit.

However, when acquiring images at a later date, volume coil images showed minimal signal on the left side when all receive channels were connected to the interface box, as shown in Figure A-4. Most importantly, this did not match the homogenous volume coil image acquired when the receive elements were statically detuned using the fan-out board. Therefore, this showed that there was an instability in the biasing signal used to actively detune the receive elements during transmit; prompting the construction of a PIN diode driver and bias tees to have more control over this biasing signal. However, due to the complexity of the setup of the PIN diode driver and bias tees, as well as the comparable SNR values achieved with this setup (not shown), our collaborators decided that using the biasing signal from the Philips interface box was the better option.
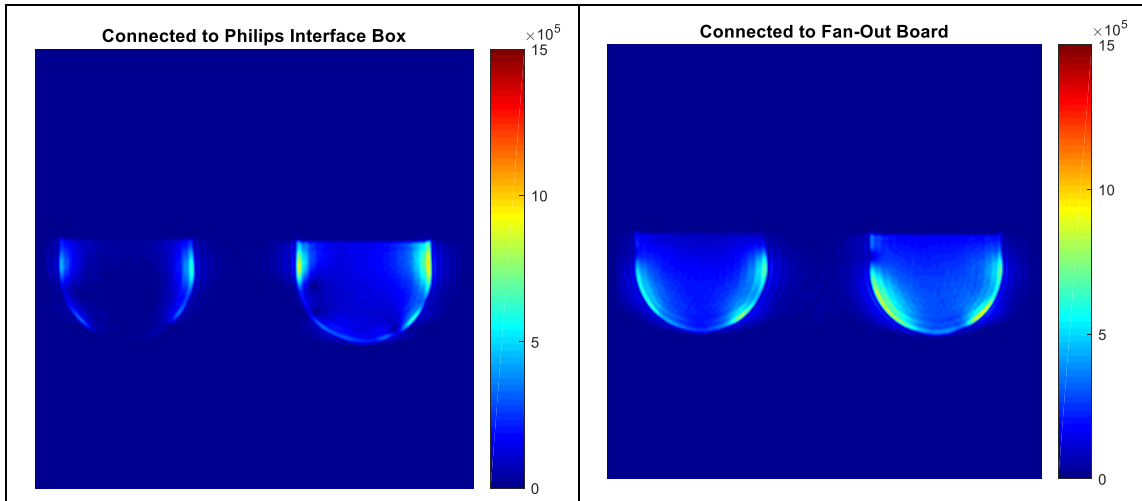
Figure A-4. Volume coil images when the receive elements were actively detuned by the Philips interface box (left) and when they were actively detuned using the fan-out board (right).